Crustal anisotropy across eastern Tibet and surroundings modeled as a depth-dependent tilted hexagonally symmetric medium

Jiayi Xie,[1] Michael H. Ritzwoller,[1] Weisen Shen[1,*] and Weitao Wang[2]

[1]*Department of Physics, University of Colorado at Boulder, Boulder, CO 80309, USA. E-mail: jiayi.xie@colorado.edu*
[2]*Institute of Geophysics, Chinese Earthquake Administration, Beijing 100045, China*

SUMMARY

Two types of surface wave anisotropy are observed regularly by seismologists but are only rarely interpreted jointly: apparent radial anisotropy, which is the difference in propagation speed between horizontally and vertically polarized waves inferred from Love and Rayleigh waves, and apparent azimuthal anisotropy, which is the directional dependence of surface wave speeds (usually Rayleigh waves). We show that a new data set of Love and Rayleigh wave isotropic phase speeds and Rayleigh wave azimuthal anisotropy observed within and surrounding eastern Tibet can be explained simultaneously by modeling the crust as a depth-dependent tilted hexagonally symmetric (THS) medium. We specify the THS medium with depth-dependent hexagonally symmetric elastic tensors tilted and rotated through dip and strike angles and estimate these quantities using a Bayesian Monte Carlo inversion to produce a 3-D model of the crust and uppermost mantle on a $0.5° \times 0.5°$ spatial grid. In the interior of eastern Tibet and in the Yunnan-Guizhou plateau, we infer a steeply dipping THS upper crustal medium overlying a shallowly dipping THS medium in the middle-to-lower crust. Such vertical stratification of anisotropy may reflect a brittle to ductile transition in which shallow fractures and faults control upper crustal anisotropy and the crystal-preferred orientation of anisotropic (perhaps micaceous) minerals governs the anisotropy of the deeper crust. In contrast, near the periphery of the Tibetan Plateau the anisotropic medium is steeply dipping throughout the entire crust, which may be caused by the reorientation of the symmetry axes of deeper crustal anisotropic minerals as crustal flows are rotated near the borders of Tibet.

Key words: Crustal imaging; Seismic anisotropy; Surface waves and free oscillations; Crustal structure.

1 INTRODUCTION

The high Tibetan Plateau has resulted from the collision of India with Eurasia over the past approximately 50 Myr (Le Fort 1975; Molnar & Tapponnier 1975; Jolivet *et al*. 1990; Hinsbergen *et al*. 2012). How the plateau has deformed in response to the collision and how it has deformed surrounding regions remains subject to debate, and has inspired a wide range of tectonic models. Hypotheses have included deformation via rigid blocks (e.g. Tapponnier *et al*. 2001), the continuous deformation of the entire lithosphere (e.g. Molnar & Tapponnier 1975; Houseman & England 1993) and flow in the lower crust (e.g. Royden *et al*. 1997).

As suggested by heat flow measurements (Francheteau *et al*. 1984) and thermokinematic models (Bollinger *et al*. 2006), the thickened Tibetan crust is believed to be hot, which implies a significant weakness of the middle and lower crust (Francheteau *et al*. 1984; Nelson *et al*. 1996; Clark & Royden 2000; Beaumont *et al*. 2001). In addition, earthquakes are mainly confined to the upper crust of eastern Tibet where brittle deformation occurs (e.g. Chu *et al*. 2009; Zhang *et al*. 2010; Sloan *et al*. 2011; Huang *et al*. 2010), seismic tomography has identified low-velocity zones in the middle-to-lower crust (e.g. Yao *et al*. 2008; Yang *et al*. 2012; Xie *et al*. 2013), and receiver function studies observe velocity contrasts in the middle crust (e.g. Kind *et al*. 2002; Nábělek *et al*. 2009; Li *et al*. 2011; Deng *et al*. 2015). Some researchers take these results as evidence for a viscously deforming deeper crust (e.g. Clark & Royden 2000; Beaumont *et al*. 2001; Shapiro *et al*. 2004), which may imply a decoupling between the upper crust and the underlying mantle. Partial melt in the middle crust may also be a common feature of central Tibet (e.g. Hacker *et al*. 2014). On the other hand, some authors argue that the Tibetan lithosphere is deforming as a coherent unit (e.g. England & Molnar 1997), at least in southern Tibet (Copley *et al*. 2011).

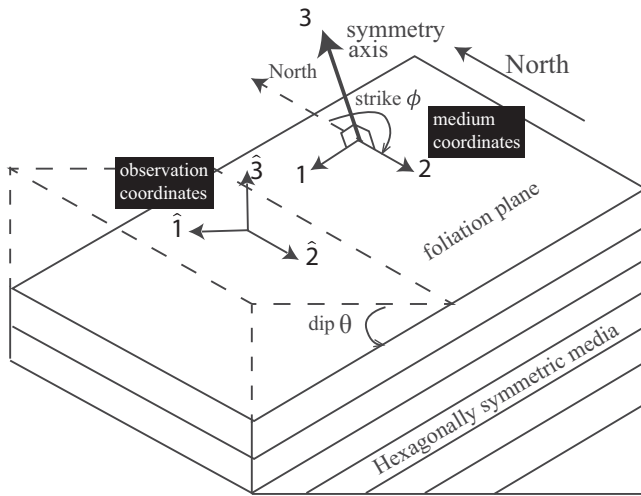*Now at: Department of Earth and Planetary Sciences, Washington University, St. Louis, MO 63130, USA.

Figure 1. Depiction of a tilted hexagonally symmetric medium (THS), showing the foliation plane, the strike and dip angles and the symmetry axis. The medium coordinates (x_1, x_2, x_3) and the observing coordinates $(\hat{x}_1, \hat{x}_2, \hat{x}_3)$ are also shown.

In this paper, we investigate the state of the upper and middle-to-lower crust of Tibet based on inferences about seismic anisotropy. There have been a number of previous studies of crustal anisotropy across Tibet based on surface waves from ambient noise or earthquake data. Radial anisotropy is the difference in propagation speed between horizontally and vertically polarized waves, inferred from Love and Rayleigh waves, respectively. Crustal radial anisotropy has been mapped across parts of Tibet by, for example, Shapiro *et al.* (2004), Chen *et al.* (2009), Duret *et al.* (2010), Huang *et al.* (2010), Guo *et al.* (2012), Xie *et al.* (2013), Agius & Lebedev (2014) and Tan *et al.* (2015). Azimuthal anisotropy characterizes how propagation speed varies with azimuth. The Rayleigh wave azimuthal anisotropy of the crust also has been mapped by Su *et al.* (2008), Yao *et al.* (2010) and Pandey *et al.* (2015).

The novelty of this study lies in its simultaneous interpretation of observations of radial and azimuthal anisotropy from surface waves by estimating the depth-dependent oriented elastic tensor in the crust. Xie *et al.* (2015), influenced by much earlier studies of Montagner & Nataf (1986, 1988) and Montagner & Jobert (1988), present a method to infer the oriented elastic tensor from such observations by imposing the constraint that the elastic tensor possesses hexagonal symmetry with an orientation (described by dip and strike angles, Fig. 1) that is constant throughout the crust. They conclude that only one dip angle (and strike angle) is needed at each location across the relatively thin crust that composes the western US. However, the Tibetan crust is much thicker and many studies have observed significant vertical complications in crustal structure, such as significant mid-crustal discontinuities (e.g. Kind *et al.* 2002; Nábělek *et al.* 2009; Li *et al.* 2011; Deng *et al.* 2015) and crustal low-velocity zones (e.g. Kind *et al.* 1996; Cotte *et al.* 1999; Rapine *et al.* 2003; Shapiro *et al.* 2004; Xu *et al.* 2007; Yao *et al.* 2008; Caldwell *et al.* 2009; Guo *et al.* 2009; Li *et al.* 2009; Acton *et al.* 2010; Jiang *et al.* 2011; Xie *et al.* 2013; Deng *et al.* 2015). Here, we consider the effects that such complications might have on the inference of the oriented elastic tensor across eastern Tibet and adjacent regions.

Estimates of the oriented elastic tensor may provide insight into the geometry of foliation of material that composes the Tibetan crust, which may provide new constraints on deformation. In par-

ticular, estimates of the elastic tensor for the crust of Tibet may provide new information about the difference or similarity between the Tibetan upper and middle-to-lower crust.

In discussing anisotropy, it is important to keep in mind two different coordinate frames (Fig. 1): the frame in which the observations are made and the frame defined by the symmetry axis of the medium. We define the elastic tensor in the coordinate frame of the medium (x_1, x_2, x_3), in which the 3-axis aligns with the symmetry axis and the coordinate pair (x_1, x_2) spans the foliation plane. We refer to anisotropy defined in this frame as '*inherent*'. In this frame, a hexagonally symmetric medium possesses no azimuthal anisotropy, where azimuth is defined in terms of rotation about the symmetry axis. In contrast, the coordinate system of observation is represented by the three components of seismometers at the Earth's surface $(\hat{x}_1, \hat{x}_2, \hat{x}_3)$ in which the 3-axis lies normal to the Earth's surface. In this frame, observations of anisotropy depend on how the components of the elastic tensor, composed of the inherent elastic moduli, are affected by the tilt of the medium (or the rotation of the symmetry axis). We refer to measurements of anisotropy and inferences drawn from them in the observational frame as '*apparent*'. Most studies of anisotropy based on surface waves have reported measurements and models of particular aspects of apparent anisotropy, such as radial and azimuthal anisotropy. In particular, azimuthal anisotropy is a commonly observed property.

The purpose of this paper is to address the following questions with a focus on eastern Tibet and surrounding areas: (1) first, can information about anisotropy contained in surface wave traveltimes observed across Tibet be fit with the oriented elastic tensor model, in the same way as similar data were fit in the western US by Xie *et al.* (2015)? (2) Second, is there a difference in anisotropy between the upper crust and middle-to-lower crust across Tibet? Specifically, is a single orientation for the elastic tensor at all depths in the crust sufficient to fit the observations? (3) Finally, does the nature and vertical distribution of anisotropy across Tibet differ from that across surrounding regions?

In order to address these questions, we combine data from three networks across parts of China and Tibet: the China Earthquake Array (CEArray), the China Array deployed in and around Yunnan Province and the PASSCAL installations in Tibet (Fig. 2b). Based on recordings from these stations, we obtain Rayleigh and Love wave phase velocity measurements from ambient noise by assimilating phase velocity measurements from previous studies and also updating Love wave phase velocity maps by introducing new observations. Rayleigh wave phase velocity maps for Tibet were previously presented by Yang *et al.* (2012), Xie *et al.* (2013) and later by Shen *et al.* (2016) who produced an isotropic and azimuthally anisotropic data set of observed surface wave phase speeds from ambient noise that covers most of China. These studies ultimately yield an integrated data set of Rayleigh wave phase speed measurements and maps, which we incorporate here. The new measurements we incorporate include both the isotropic and azimuthally anisotropic components of Rayleigh wave phase speeds (Fig. 3). Xie *et al.* (2013) present isotropic Love wave phase speed maps for Tibet. Here, we add new measurements of Love wave phase speeds based on ambient noise recorded at 438 China Array stations in and around Yunnan Province, and produce updated Love wave phase speed maps.

The remainder of this paper is separated into five principal sections. In Section 2, we briefly describe the data used in our inversion, which is period-dependent surface wave phase speeds extracted from Rayleigh and Love wave tomography, including data
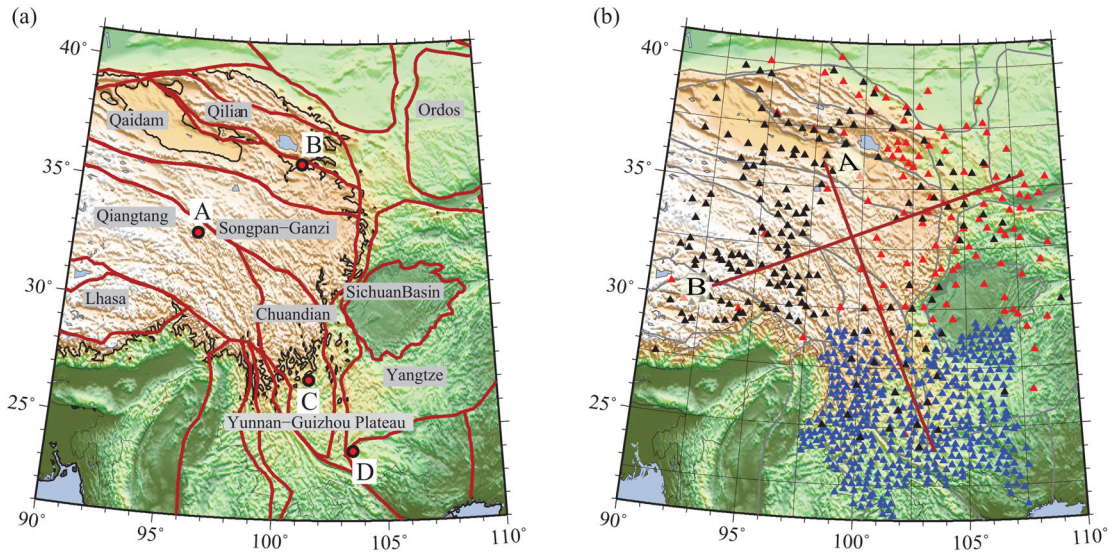
Figure 2. (a) Reference map of the study region in which 3 km topography isolines are presented (black lines) along with the boundaries of major geological units (red lines). Points A–D indicate sample locations referenced in Figs 5, 8–11, 17 and 21. (b) Locations of seismic stations used in this study: CEArray stations (red triangles), China Array stations around Yunnan province (blue triangles) and PASSCAL stations (black triangle). The two profiles (A, B) are used in Figs 14 and 19.
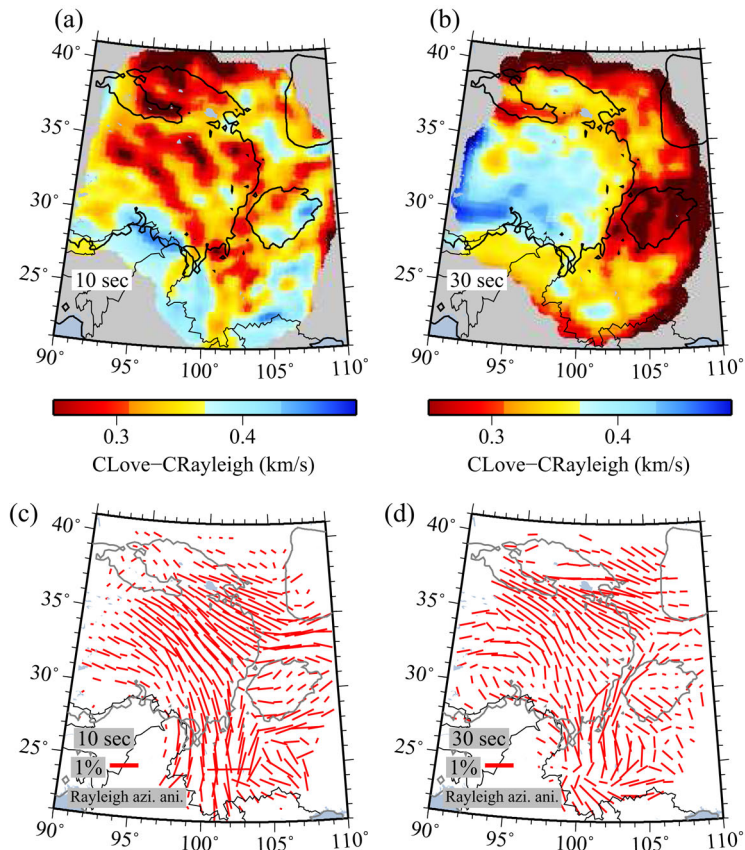

Figure 3. (a) and (b) Examples of the Love–Rayleigh phase speed difference ($C_{Love} - C_{Rayleigh}$) across the study region at periods of 10 and 30 s. (c) and (d) The observed Rayleigh wave 2ψ ($180°$ periodicity) azimuthal anisotropy maps at 10 and 30 s periods. The red bars identify Rayleigh wave fast orientations with lengths proportional to the amplitude in percent (a_2 in eq. 1).

sensitivity and uncertainties. In Section 3, we clarify the terminology and concepts that underlie our work, particularly as related to the notions of inherent and apparent anisotropy. In Section 4, we describe the model parametrization and constraints applied in the

Bayesian Monte Carlo inversion. In Section 5, we describe the model of the depth-dependent tilted elastic tensor in the crust that explains this data set and present views with horizontal maps and vertical profiles of the estimated dip and inherent strength of anisotropy

and their uncertainties. In Section 6, we provide views of apparent anisotropy to aid comparison with previous studies and discuss the physical and geological significance of the results.

2 DATA

2.1 Measurements

In this study, we combine new ambient noise-based Love wave phase velocity measurements with previously observed Rayleigh and Love wave phase speed measurements obtained from cross-correlations of continuous ambient noise data. First, for Rayleigh waves, we incorporate the subset of the maps of isotropic and azimuthally anisotropic phase velocities from Shen *et al*. (2016) that covers our study area. Shen *et al*. (2016) produce isotropic Rayleigh wave phase speed maps (8–50 s period) using ray theoretic tomography (Barmin *et al*. 2001), and simultaneously estimate maps of azimuthal anisotropy. Second, we also incorporate the isotropic Love wave phase speed measurements obtained by Xie *et al*. (2013) using ambient noise cross-correlations based on CEArray and PASSCAL data. Finally, we introduce new Love wave phase speed measurements obtained from cross-correlations of ambient noise recorded at the 438 China Array stations centred on Yunnan Province. The Love wave phase velocity measurements for each cross-correlation station pair are measured using automated frequency–time analysis (Levshin & Ritzwoller 2001; Bensen *et al*. 2007) as in the study of Xie *et al*. (2013). We apply ray theoretic tomography (Barmin *et al*. 2001) to generate azimuthally variable and isotropic Love wave phase velocity maps from 8 to 40 s period.

In a weakly anisotropic medium, the azimuthal dependence of phase velocity for a Rayleigh wave has the following form (Smith & Dahlen 1973):

$$C(T, \psi) = C_0(T)[1 + a_2 \cos(2(\psi - \varphi_{FA})) + a_4 \cos(4(\psi - \alpha))]$$

(1)

where T is period, ψ is the azimuth of propagation of the wave measured clockwise from north, $C_0(T)$ is the isotropic phase speed, φ_{FA} is the 2ψ fast-axis orientation, α is an analogous angle for the 4ψ variation in phase velocity and a_2 and a_4 are the relative amplitudes of the 2ψ and 4ψ anisotropy. Based on theoretical arguments (Smith & Dahlen 1973; Montagner & Nataf 1986) and observations (e.g. Lin & Ritzwoller 2011; Lin *et al*. 2011; Xie *et al*. 2015), the 2ψ term (180° periodicity) is understood to dominate the Rayleigh wave azimuthal variation, so we will only present the 2ψ signal here for Rayleigh waves. In contrast, Love wave azimuthal anisotropy is dominated by the 4ψ term (90° periodicity), which means that exceptionally good azimuthal coverage is required for Love wave anisotropy to be measured reliably. Because the azimuthal coverage is not ideal across much of Tibet and because Love wave observations are typically noisier than Rayleigh wave observations, we do not use the azimuthal anisotropy observed for Love waves in the inversion presented here.

We produce isotropic phase speed maps for Love waves (8–40 s period) and Rayleigh waves (8–50 s period), and 2ψ azimuthal anisotropy maps for Rayleigh waves (8–50 s period). Examples of the difference between the isotropic parts of Love and Rayleigh wave phase speeds are shown in Figs 3(a) and (b) at periods of 10 and 30 s. Love wave phase speeds are everywhere faster than Rayleigh wave speeds in the period band of measurement, but the difference between Love and Rayleigh wave speeds (referred to as $C_{Love} - C_{Rayleigh}$ in Fig. 3) depends on period and location. Examples

of Rayleigh wave azimuthally anisotropic phase velocity maps are presented in Figs 3(c) and (d) at 10 and 30 s period, where the length of each bar is the amplitude of 2ψ anisotropy (a_2 in eq. 1, in percent), and the orientation of each bar is the fast-axis orientation (φ_{FA} in eq. 1). The azimuthal anisotropy has large amplitudes within Tibet and in the Yunnan-Guizhou plateau south of the Sichuan basin. At short periods, fast-axis directions generally follow the orientations of surface faults.

2.2 Data sensitivity

The differences between Love and Rayleigh wave phase speeds shown in Figs 3(a) and (b) reflect the amplitude of the Rayleigh–Love discrepancy in our observations and provide information about the depth distribution of *S*-wave anisotropy. The Rayleigh–Love discrepancy is a measure of the inability of a simply parametrized isotropic model to fit Rayleigh and Love wave dispersion curves simultaneously. The introduction of radial anisotropy, or the speed difference between horizontally polarized (V_{SH}) and vertically polarized (V_{SV}) waves in a transversely isotropic (TI) medium (hexagonally symmetric medium with a vertical symmetry axis), is one way to resolve the Rayleigh–Love discrepancy. In general, the phase speed difference between Love and Rayleigh waves increases within the eastern Tibetan Plateau up to about a period of 30 s, and decreases or remains nearly constant with period outside of the Plateau. Procedurally, we specify anisotropy with the elastic tensor and its orientation, and use the notation V_{PV}, V_{PH}, V_{SH} and V_{SV} only when speaking of a TI medium. In a medium with a tilted symmetry axis, we will specify anisotropy exclusively in terms of the Love moduli *A*, *C*, *N*, *L* and *F*.

Synthetic examples of the difference between Love and Rayleigh wave phase speeds are shown in Figs 4(a) and (b). Four models of the depth distribution of the difference between V_{sh} and V_{sv} in a TI medium are shown in Fig. 4(a) and the resulting differences between Love and Rayleigh wave phase speeds ($C_{Love} - C_{Rayleigh}$) are shown in Fig. 4(b), which depend strongly on the amplitude and depth distribution of the difference $V_{SH} - V_{SV}$. For example, comparing the two models in which one is isotropic (green line, Fig. 4a) and the other has a depth constant radial anisotropy ($V_{SH} - V_{SV} = 5$ per cent, black line, Fig. 4b) in the crust, there is a difference in $C_{Love} - C_{Rayleigh}$ of more than 200 m s^{-1}, which is a very large effect. The concentration of radial anisotropy in progressively shallower and deeper depth ranges in the crust has a progressively decreasing effect on the Love–Rayleigh phase speed difference. The shapes of the curves in Fig. 4(b) depend on several factors. The period of the peak difference between Love and Rayleigh wave phase speeds depends largely on crustal thickness. The negative slope of the curves at periods longer than the peak period occurs because the Rayleigh wave becomes sensitive to the mantle at shorter periods than the Love wave. The upward curve at the longest periods occurs because of increasing sensitivity of Love waves to mantle anisotropy.

As discussed further in Section 3, a TI medium can be characterized with five elastic moduli. Rayleigh and Love waves are differentially sensitive to these five moduli, which can be represented with the Love parameters *A*, *C*, *N*, *L* and *F* or V_{SV}, V_{SH}, V_{PV}, V_{PH} and η. As Figs 4(c) and (d) illustrate, Rayleigh waves are predominantly sensitive to V_{SV} and Love waves are almost entirely sensitive to V_{sh}. Rayleigh waves also possess substantial sensitivity to η and to both V_{PV} and V_{PH}, although the V_{PV} and V_{PH} sensitivities tend to cancel one another which results in a sensitivity to V_{PV}
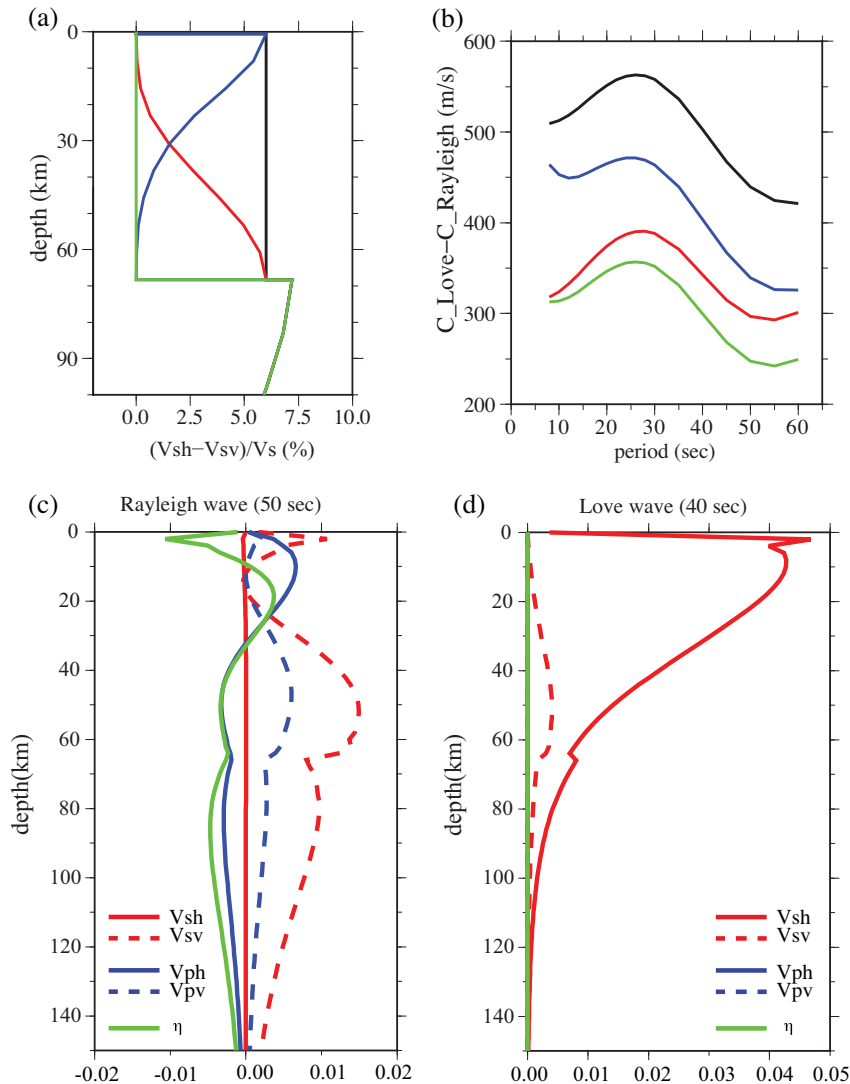
Figure 4. (a) and (b) Simulations that illustrate the effect of changes in a hexagonally symmetric medium with a vertical symmetry axis (a TI or a VHS medium) on the Love–Rayleigh phase speed difference. (a) Four types of structures with different amplitudes of radial anisotropy ($V_{SH} - V_{SV}$ in per cent) in the crust but with the same anisotropy in the mantle. (b) The Love–Rayleigh phase speed differences ($C_{Love} - C_{Rayleigh}$) computed from the structures shown in (a). (c) and (d) Example unnormalized sensitivity kernels for Rayleigh and Love wave phase velocities for a VHS medium: 50 s period for Rayleigh waves with perturbations in V_{SV}, V_{SH}, V_{PV}, V_{PH} and η, as a function of depth, and 40 s period for Love waves with perturbations in V_{SH} and V_{SV}.

that is much weaker and more shallow than to V_{SV}. Love waves are sensitive to shallower structures than Rayleigh waves at a given period, the effect of which is amplified in this study because our Love wave measurements only extend up to 40 s period whereas the Rayleigh waves extend to 50 s. The sensitivity kernels in Figs 4(c) and (d) are at the longest periods of this study. Love wave phase speed sensitivity at 40 s period extends only to about 50 km depth (at 25 per cent of the maximum amplitude of the sensitivity curve), whereas Rayleigh wave sensitivity at 50 s period extends to greater than 100 km (based on the same relative amplitude criterion). This difference in depth sensitivity of Love and Rayleigh waves has implications for the reliability of estimates of anisotropy, as discussed in Section 6.3.1.

In the inversion for the elastic tensor, the differential sensitivity of Rayleigh and Love waves to the elastic moduli allows only some of the moduli to be estimated well. This is complicated further by the need to estimate the dip and rotation angles for the elastic tensor. An important aspect of the Bayesian Monte Carlo inversion procedure

described later is to estimate the relative precision with which the different moduli and rotation angles can be estimated.

2.3 Uncertainty estimates

Because eikonal tomography (Lin *et al.* 2009) models off great circle propagation and provides an estimate of uncertainty, everything else being equal we would prefer to use it rather than the traditional ray theoretic tomography that we apply here (Barmin *et al.* 2001). However, eikonal tomography does not perform well in the presence of spatial gaps in the station coverage such as those found in eastern Tibet. Such spatial gaps prevent us from constructing accurate phase velocity maps and uncertainty estimates using eikonal tomography across much of the study region. Thus, our uncertainty estimates for the isotropic phase velocity maps (Love and Rayleigh waves) and azimuthal anisotropy maps (Rayleigh wave) are based on the spatially averaged 1σ uncertainty estimates obtained by applying eikonal tomography where the method does work in the region of
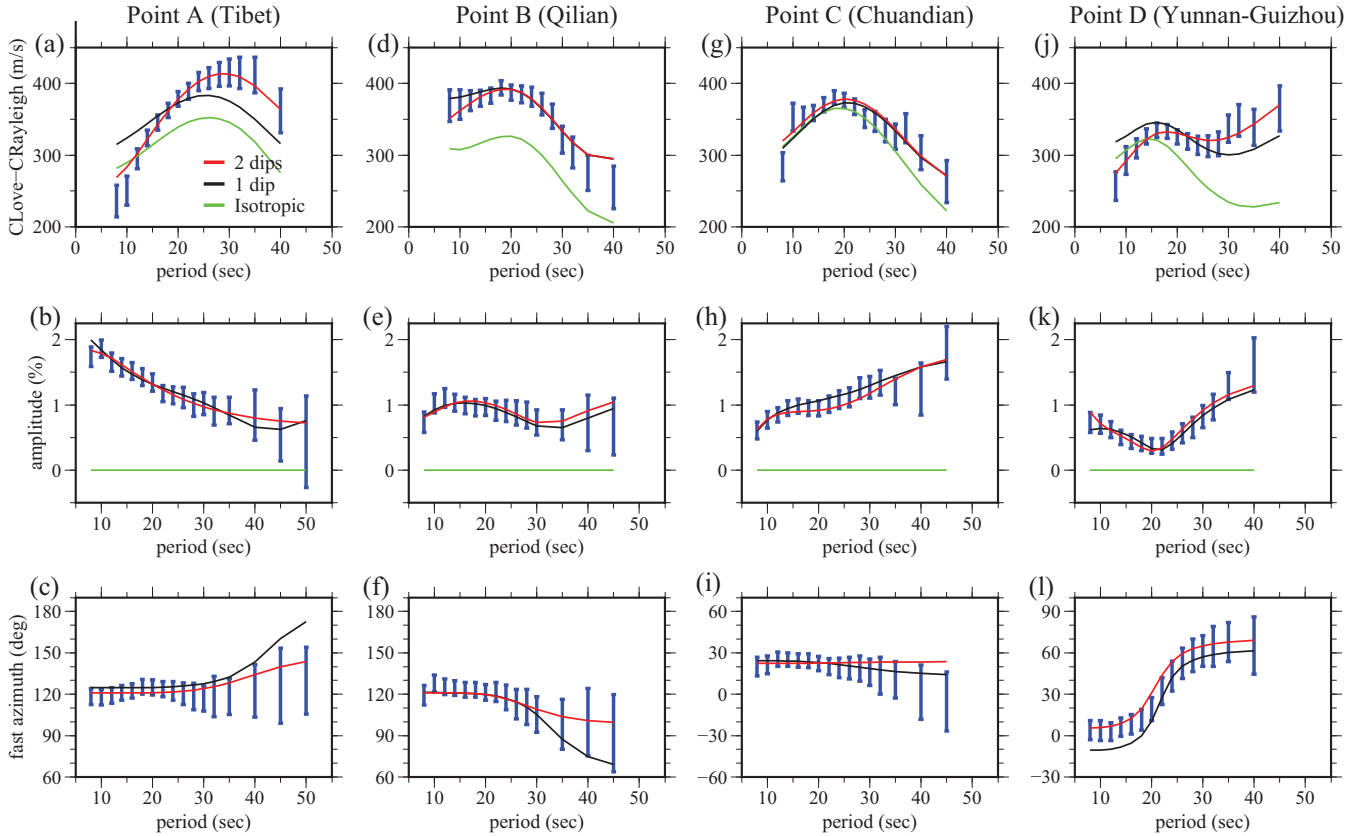
Figure 5. Surface wave measurements presented as 1σ error bars illustrating model fits at four locations: eastern Tibet (Point A), Qilian terrane (Point B), Chuandian terrane (Point C) and Yunan-Guizhou plateau (Point D) identified in Fig. 2(a). (a), (d), (g) and (j) Love minus Rayleigh wave phase speed. (b), (e), (h) and (k) Amplitude of Rayleigh wave azimuthal anisotropy (coefficient a_2 in eq. 1). (c), (f), (i) and (l) Rayleigh wave fast-axis orientation. The solid lines are curves computed from the best-fitting model at the location using three model parametrizations: isotropic model (green lines), tilted hexagonally symmetric (THS) model with a constant dip angle in the crust (black lines) and THS model with two dip angles in the crust (red lines). Aspects of the THS models with two crustal dip angles are shown in Fig. 11.

study. Where eikonal tomography does not work well we scale up the spatially averaged uncertainty. To do this, we are motivated by the procedure described at greater length by Shen *et al*. (2016). We scale the measurement uncertainties based on a combination of three factors: resolution, ray-path azimuthal coverage and the amplitude of azimuthal anisotropy. The uncertainties for Rayleigh and Love wave isotropic phase speed maps are scaled using resolution alone as a guide, as described by Shen *et al*. (2016). The uncertainty for Rayleigh wave azimuthal anisotropy amplitude is scaled using both resolution and azimuthal coverage. Uncertainty for the Rayleigh wave azimuthal anisotropy fast axis is scaled using all three factors. Examples of uncertainties in measured quantities are presented as one standard deviation error bars in Fig. 5.

2.4 Dispersion curves

From the Love wave (8–40 s period) and Rayleigh wave (8–50 s period) isotropic phase speed maps, the Rayleigh wave azimuthal anisotropy maps and their uncertainties, we generate at all locations on a 0.5° × 0.5° grid across the study region isotropic phase speed curves for both Rayleigh and Love waves and period-dependent curves of the amplitude and fast-axis orientation of Rayleigh wave azimuthal anisotropy. These four local curves form the basis for the 3-D model inversion described later in the paper.

Fig. 5 presents examples of these local dispersion curves at the four locations identified in Fig. 2(a) (A: eastern Tibet, B: Qilian ter-

rane, C: Chuandian terrane just off the Tibetan plateau, E: Yunan-Guizhou plateau). Instead of showing the Love and Rayleigh wave isotropic phase speed curves separately, we present the difference between them as in the simulation results presented in Fig. 4(b), although in the inversion they are used as two independent observations. Phase speed differences are presented as error bars, defined as the square root of the sum of the squares of the estimated uncertainties of the Rayleigh and Love wave phase speeds at each location. As shown in Fig. 5(a), within Tibet the difference between Love and Rayleigh wave phase speeds increases rapidly to peak at about 30 s period and decreases slowly at longer periods. Outside of Tibet (Figs 5d, g and j), the difference increases at short periods less rapidly than in Tibet, peaks at a shorter period, and then decreases either quicker or remains flat with period. A comparison of the synthetic curves in Fig. 4(b) with the observations in Figs 5(a), (d), (g) and (j) provides hints to the depth distribution of radial anisotropy in Tibet and regions surrounding it.

In addition, the middle and bottom rows of Fig. 5 show the period-dependent curves for the amplitude and fast-axis orientation of Rayleigh wave 2ψ azimuthal anisotropy, respectively. The features of these curves vary dramatically from place to place. For example, at Point A (eastern Tibet), the amplitude of Rayleigh wave azimuthal anisotropy decreases with period and the Rayleigh wave fast azimuth does not change strongly with period. In contrast, at Point B (Qilian terrane), the amplitude of Rayleigh wave azimuthal anisotropy remains flat with period but the Rayleigh wave fast

azimuth changes moderately with period. At Points C and D, azimuthal anisotropy changes in still different ways with period. At Point C, the amplitude of anisotropy increases with period, and at Point D, the fast-axis orientation differs appreciably between short and long periods, which indicates a change in the orientation of anisotropy with depth.

3 BACKGROUND: TERMINOLOGY FOR A HEXAGONALLY SYMMETRIC MEDIUM

The spatially dependent isotropic and azimuthally anisotropic phase velocity measurements described above provide information about the isotropic and anisotropic properties of the crust and uppermost mantle. The properties of an elastic medium and seismic wave velocities depend on the depth-dependent constitution and orientation of the elastic tensor, which consists of 21 independent components for a general anisotropic medium. Simplifications are needed in order to constrain aspects of the elastic tensor. A useful starting point is the assumption that the medium possesses hexagonal symmetry, which at each depth is described by five unique elastic moduli known as the Love moduli: A, C, N, L and F (Montagner & Nataf 1988; Xie *et al*. 2015). A and C are compressional moduli and N and L are shear moduli. The Voigt simplification of the elastic tensor is the 6×6 elastic modulus matrix, $C_{\alpha\beta}$, which for a hexagonally symmetric medium with a vertical symmetry axis is given by:

$$^{V}C_{\alpha\beta} = \begin{bmatrix} A & A-2N & F & 0 & 0 & 0 \\ A-2N & A & F & 0 & 0 & 0 \\ F & F & C & 0 & 0 & 0 \\ 0 & 0 & 0 & L & 0 & 0 \\ 0 & 0 & 0 & 0 & L & 0 \\ 0 & 0 & 0 & 0 & 0 & N \end{bmatrix} \quad (2)$$

where the V superscript denotes 'vertical' for the orientation of the symmetry axis. With a vertical symmetry axis, a hexagonally symmetric medium will produce no azimuthal variation is surface wave speeds. A hexagonally symmetric medium may possess either a slow or fast symmetry axis; the slow symmetry case occurs when $C < A$ and $L < N$, which crustal rocks generally display and finely layered media require (e.g. Brownlee *et al*. 2011; Erdman *et al*. 2013; Thomsen & Anderson 2015).

A hexagonally symmetric medium with a vertical symmetry axis or TI medium is unique in that the 3-axis of the medium coordinates (symmetry axis) coincides with the 3-axis of the observing coordinates (vertical direction), as defined in Fig. 1. For a TI medium, four of the five Love moduli are directly related to *P*- and *S*-wave speeds for waves propagating vertically or horizontally in the Earth: $A = \rho V^2_{PH}$, $C = \rho V^2_{PV}$, $L = \rho V^2_{SV}$, $N = \rho V^2_{SH}$. Here, ρ is density, V_{PH} and V_{PV} are the speeds of *P* waves propagating horizontally and vertically in the Earth, V_{SV} is the speed of the *S* wave propagating horizontally and polarized vertically or propagating vertically and polarized horizontally and V_{SH} is the speed of the *S* wave that is propagating in a horizontal direction and polarized horizontally. The modulus $F = \eta(A - 2L)$ affects the speed of waves propagating oblique to the symmetry axis and controls the shape of the shear wave phase speed surface (Okaya & Christensen 2002). For an isotropic medium, $A = C$, $L = N$, $F = A - 2L$, $\eta = 1$.

Hexagonally symmetric earth media may have a non-vertical, tilted and rotated symmetry axis as illustrated in Fig. 1, where the tilt is denoted by the dip angle θ and the rotation by the strike angle ϕ. We use the notation V_{PH}, V_{PV}, V_{SV} and V_{SH} only when discussing a medium with a vertical symmetry axis or an isotropic medium. With a tilted symmetry axis, we will use the notation A, C, N, L and F (or $\eta = F/(A - 2L)$) to represent the elements of the elastic tensor. We also introduce the following terminology: VHS for a hexagonally symmetric medium with a vertical symmetry axis, HHS for a hexagonally symmetric medium with a horizontal symmetry axis and THS for a hexagonally symmetric medium with a tilted symmetry axis.

A rotation of the medium will rotate the elastic tensor in eq. (2) to produce the modulus matrix $C_{\alpha\beta}(\theta, \phi)$. We refer to a general reorientation of the symmetry axis as a tilt, which is achieved by pre- and post-multiplying the elastic modulus matrix by the appropriate rotation matrix and its transpose, respectively (e.g. Auld 1973; Carcione 2007), which act to rotate the fourth-order elasticity tensor appropriately. The rotation can fill all components of the modulus matrix but will preserve its symmetry:

$$C_{\alpha\beta}(\theta, \phi) = \begin{bmatrix} C_{11} & C_{12} & C_{13} & C_{14} & C_{15} & C_{16} \\ C_{12} & C_{22} & C_{23} & C_{24} & C_{25} & C_{26} \\ C_{13} & C_{23} & C_{33} & C_{34} & C_{35} & C_{36} \\ C_{14} & C_{24} & C_{34} & C_{44} & C_{45} & C_{46} \\ C_{15} & C_{25} & C_{35} & C_{45} & C_{55} & C_{56} \\ C_{16} & C_{26} & C_{36} & C_{46} & C_{56} & C_{66} \end{bmatrix} \quad (3)$$

Montagner & Nataf (1986) showed that this modulus matrix may be decomposed into azimuthally independent and azimuthally dependent parts as follows:

$$C_{\alpha\beta}(\theta, \phi) = \begin{bmatrix} \hat{A} & \hat{A}-2\hat{N} & \hat{F} & 0 & 0 & 0 \\ \hat{A}-2\hat{N} & \hat{A} & \hat{F} & 0 & 0 & 0 \\ \hat{F} & \hat{F} & \hat{C} & 0 & 0 & 0 \\ 0 & 0 & 0 & \hat{L} & 0 & 0 \\ 0 & 0 & 0 & 0 & \hat{L} & 0 \\ 0 & 0 & 0 & 0 & 0 & \hat{N} \end{bmatrix}$$

$$+ \begin{bmatrix} \delta C_{11} & \delta C_{12} & \delta C_{13} & \delta C_{14} & \delta C_{15} & \delta C_{16} \\ \delta C_{12} & \delta C_{22} & \delta C_{23} & \delta C_{24} & \delta C_{25} & \delta C_{26} \\ \delta C_{13} & \delta C_{23} & \delta C_{33} & \delta C_{34} & \delta C_{35} & \delta C_{36} \\ \delta C_{14} & \delta C_{24} & \delta C_{34} & \delta C_{44} & \delta C_{45} & \delta C_{46} \\ \delta C_{15} & \delta C_{25} & \delta C_{35} & \delta C_{45} & \delta C_{55} & \delta C_{56} \\ \delta C_{16} & \delta C_{26} & \delta C_{36} & \delta C_{46} & \delta C_{56} & \delta C_{66} \end{bmatrix} \quad (4)$$

where $\hat{A} = 2(C_{11} + C_{22})/8 + C_{12}/4 + C_{66}/2$, $\hat{C} = C_{33}$, $\hat{N} = (C_{11} + C_{22})/8 - C_{12}/4 + C_{66}/2$, $\hat{L} = (C_{44} + C_{55})/2$ and $\hat{F} = (C_{13} + C_{23})/2$. The carat over the symbols indicates that the moduli are azimuthal averages, and can be thought of as the apparent radially anisotropic moduli that would be observed in the observing coordinates. Apparent azimuthally averaged seismic velocities can be defined similarly:

$$\hat{V}_{SH} = \sqrt{\hat{N} \big/ \rho}, \hat{V}_{SV} = \sqrt{\hat{L} \big/ \rho}, \hat{V}_{PH} = \sqrt{\hat{A} \big/ \rho}, \hat{V}_{PV} = \sqrt{\hat{C} \big/ \rho}.$$

As discussed in the Introduction, it is important to distinguish between the coordinates used to describe the medium's properties and the coordinates in which the observations are made. We define anisotropy in the coordinate system of the medium in which the 3-axis is parallel to the medium's symmetry axis and the 1- and 2-axes lie in the foliation plane as shown in Fig. 1. In these coordinates, the five Love moduli completely describe the anisotropy, and because the medium is hexagonally symmetric there is no (inherent) azimuthal anisotropy. Following Xie *et al*. (2015), we refer to anisotropy in the coordinate frame of the medium as 'inherent'. To describe the anisotropy fully, we include the medium's orientation by specifying the dip and strike angles.

Thomsen (1986) defined useful summaries of inherent anisotropy:

$$\gamma \equiv \frac{N-L}{2L} \quad \varepsilon \equiv \frac{A-C}{2C} \quad \delta \approx \frac{F+2L-C}{C} \quad (5)$$

where, in particular, we refer to γ as 'inherent *S*-wave anisotropy'. In contrast, in the observing coordinates the description of anisotropy is 'apparent'. The azimuthally averaged elastic tensor, given by the first matrix on the right-hand side of eq. (4), summarizes the apparent radial anisotropy of the medium, which depends both on the inherent moduli and the dip angle. As defined by Xie *et al.* (2015), a useful description is the apparent *S*-wave radial anisotropy:

$$\hat{\gamma} \equiv \frac{\hat{N}-\hat{L}}{2\hat{L}} \quad (6)$$

where, as in eq. (4), the carat over a symbol indicates that the quantity is apparent. Apparent *S*-wave radial anisotropy is what most studies refer to simply as 'radial anisotropy' (e.g. Shapiro *et al.* 2004; Xie *et al.* 2015). Although there is no inherent azimuthal anisotropy in our model, apparent Rayleigh (or *SV*) wave azimuthal anisotropy emerges in the observing frame by tilting the medium, which we represent with dimensionless amplitude:

$$\hat{\Gamma} \equiv \frac{\left((C_{55}-C_{44})^2 + (C_{45})^2\right)^{1/2}}{2\hat{L}} \quad (7)$$

and direction $\hat{\varphi}_{FA} = \frac{1}{2}\tan^{-1}(C_{45}/(C_{55}-C_{44}))$. $\hat{\Gamma}$ is equivalent to $|G|/2L$ used in other studies (e.g. Yao *et al.* 2010; Lin *et al.* 2011; Yuan *et al.* 2011; Xie *et al.* 2015).

Thus, the anisotropy of a THS medium can be described completely in terms of the inherent Love moduli and the dip angle. Alternately, it can be described partially by the apparent radial and azimuthal anisotropy, which depend on the inherent anisotropy and tilt. In particular, for the same inherent elastic tensor, the nature of the apparent anisotropy will depend on the orientation of the medium. Fig. 6 demonstrates qualitatively how apparent *SV*-wave (or Rayleigh wave) azimuthal anisotropy, $\hat{\Gamma}$, and apparent *S*-wave radial anisotropy, $\hat{\gamma}$, will vary as a function of the dip angle of the symmetry axis. These curves are computed from a simple elastic tensor with a slow vertical symmetry axis with inherent *S*-wave anisotropy γ normalized to unity. For this model, the amplitude of apparent azimuthal anisotropy $\hat{\Gamma}$ increases monotonically with increasing dip angle θ, and the apparent radial anisotropy $\hat{\gamma}$ decreases with increasing dip. When the foliation plane is flat or equivalently the symmetry axis is vertical (dip $\theta = 0°$), there is strong positive apparent *S*-wave radial anisotropy but no azimuthal anisotropy. As the dip angle increases, the apparent radial anisotropy becomes negative and azimuthal anisotropy attains its maximum value.

Observations of strong positive apparent radial anisotropy but low amplitude apparent azimuthal anisotropy are consistent with a subhorizontal foliation plane and a slow nearly vertical symmetry axis (i.e. a VHS medium). In contrast, observations of a strongly negative apparent radial anisotropy and strong azimuthal anisotropy are consistent with a subhorizontal symmetry axis (i.e. an HHS medium). Simultaneous observations of intermediate values of radial and azimuthal anisotropy are consistent with a tilted symmetry axis (i.e. a THS medium). Therefore, technically, with surface wave observations, we can invert for a description of the THS medium. However, because surface waves are strongly sensitive only to a subset of the seven depth-depdendent variables that describe the THS medium, a straightforward inversion is impractical with surface wave data alone. Following Xie *et al.* (2015), we employ a Bayesian Monte
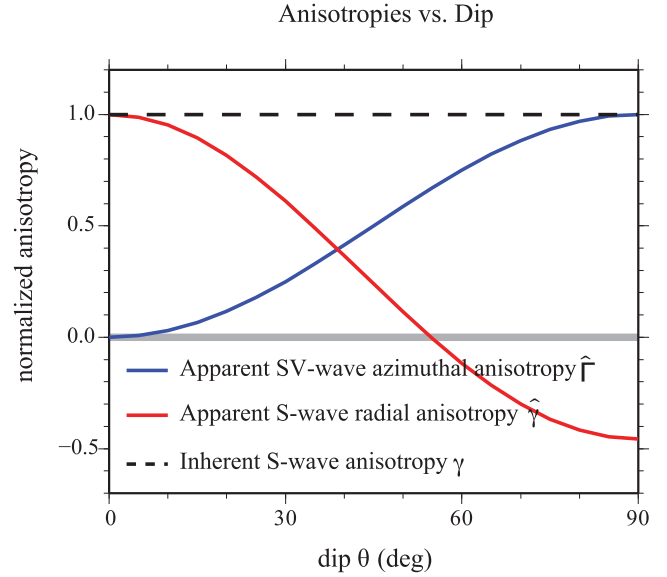

Anisotropies vs. Dip

Figure 6. Variation of apparent *S*-wave radial anisotropy $\hat{\gamma}$ (red curve) and apparent *SV*-wave azimuthal anisotropy $\hat{\Gamma}$ (blue curve) as a function of dip angle θ. The inherent *S*-wave anisotropy γ is constant and normalized to unity. This computation results from a simplified hexagonally symmetric elastic tensor, details of these functions will depend on the form of the elastic tensor.

Carlo inversion method to estimate distributions of THS parameters that agree with the data. Such posterior distributions reflect both variances within and covariances between all model variables. Here, we present models in terms of inherent anisotropy and the dip and strike angles, but because most studies present apparent radial anisotropy and apparent azimuthal anisotropy we also convert our results into these quantities to aid comparison with other studies (Section 6.1).

4 MODEL SPECIFICATION: PARAMETRIZATION AND CONSTRAINTS

Fig. 7 schematically represents the model parametrization, which is similar in many respects to the parametrization applied by Xie *et al.* (2015). Like Xie *et al.* (2015), we parametrize the crust in terms of a depth-varying THS medium that is described by seven inherent parameters (A, C, N, L, F, strike ϕ and dip θ) (Fig. 1). The depth dependences of the elastic moduli A, C, N, L and F are represented by five B-splines in the crystalline crust from the base of the sediments to Moho. For Xie *et al.* (2015), at each location, the dip and strike angles (tilt angles θ, ϕ) that define the orientation of the symmetry axis of anisotropy are constant through the crystalline crust. Here, however, we introduce a discontinuity in the crust that allows the dip angle to change gradually from values above and below a mid-crustal dip boundary set at one-third of the crystalline crustal thickness at each location. The strike angle, however, remains constant throughout the crust. Like Xie *et al.* (2015), we assume the sediments to be isotropic. We constrain crustal anisotropy to have a slow symmetry axis consistent with studies of crustal petrology as discussed in Section 6.2.2. In addition, we find that the introduction of a fast symmetry axis tends to be incompatible with the frequency dependence of our observations.
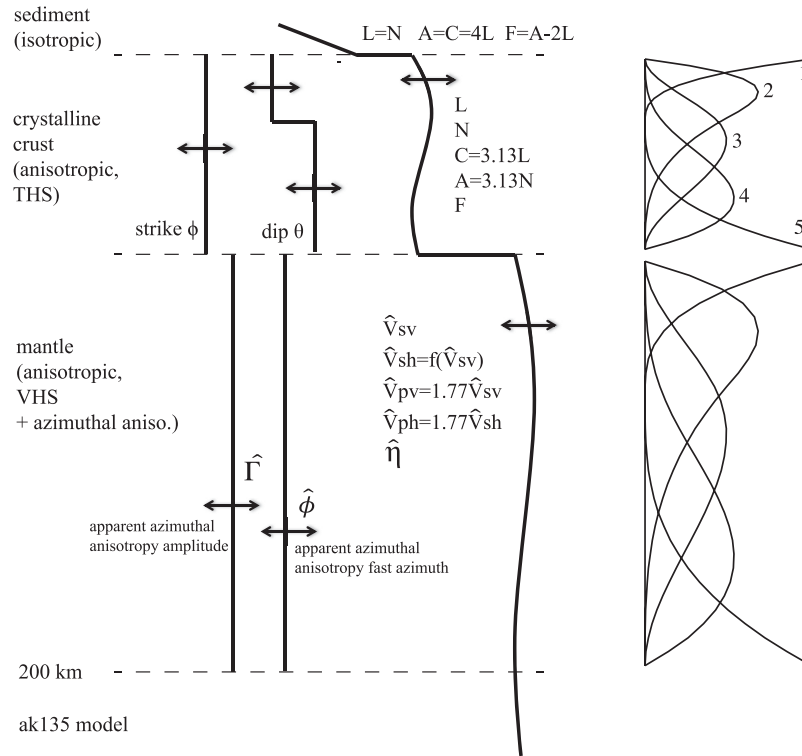
Figure 7. Model parametrization. Sedimentary structure is isotropic with shear and compressional velocities increasing linearly with depth. The crystalline crust is an anisotropic THS medium described by seven depth-dependent parameters at each depth: five inherent elastic moduli, dip angle and strike angle. The elastic moduli change smoothly with depth and are represented with five B-splines. Strike is constant within the crystalline crust and dip is allowed to change once within the crystalline crust at a depth of one-third of the crustal thickness. The uppermost mantle is modeled as a VHS anisotropic medium plus apparent azimuthal anisotropy and is described by seven parameters: five apparent elastic moduli ($\hat{V}_{SV}$, $\hat{V}_{SH}$, $\hat{V}_{PV}$, $\hat{V}_{PH}$, $\hat{\eta}$) and two parameters to represent apparent azimuthal anisotropy ($\hat{\Gamma}$, $\hat{\phi}$). Mantle apparent radial anisotropy $\hat{\gamma}$ is constrained to be 4.5 per cent and the amplitude of mantle apparent azimuthal anisotropy is constant with depth.

We introduce a sharp mid-crustal vertical gradient in dip angle, referred to here for simplicity as a discontinuity, because we find that we are unable to fit our observations over large areas, particularly in Tibet, without it. Fig. 5 illustrates this point. The difference between Love and Rayleigh wave phase speeds at Point A in Tibet (Fig. 5a) cannot be fit with a model in which the dip angle is constant in the crust (black line, 1-dip), but can be fit when we allow dip angle to change once discontinuously in the crust (red line, 2-dip). We choose the value of one-third of the crustal thickness as the location of the discontinuity in accordance with the study of Deng *et al*. (2015), who observed a discontinuity at about this depth in northern Tibet based on joint inversion of surface wave dispersion and receiver function data. In contrast, in some areas, the data can be fit by the model with a constant crustal dip, such as Points B and C in the Qilian and Chuandian terranes (Figs 5b and g). At Point D in the Yunnan-Guizhou plateau (Fig. 5j), two crustal dip angles are needed to fit the data but the misfit produced by the single dip model is not as large as within Tibet.

We use the China reference model produced by Shen *et al*. (2016) as the crustal reference around which perturbations are applied in the inversion. This is an isotropic model based on Rayleigh wave data, which most strongly constrain the elastic modulus L (related to V_{SV} in a TI medium). We use the model to define a reference for the four elastic moduli and density: $A_0(r)$, $C_0(r)$, $N_0(r)$, $L_0(r)$ and $\rho_0(r)$, where r is the radius within the Earth. Also, we use it to define sedimentary structure (seismic velocities and density increase linearly with depth and thickness), Moho depth and $Q(r)$, which we do not change in the inversion.

Based on data sensitivity (e.g. Figs 4c and d), we apply several prior constraints to the seven depth-dependent parameters that describe the oriented elastic tensor. We apply weaker constraints on parameters to which data are highly sensitive, and stronger constraints on parameters to which the data have little sensitivity. Therefore, the shear moduli L and N are relatively weakly constrained, and are perturbed within the range of $L_0(1 \pm 0.3)$. In contrast, the compressional moduli are strongly constrained, and we set $C = (1.77)^2$ $L \approx 3.13 N$ where 1.77 is the Vp/Vs ratio, and similarly we set $A = (1.77)^2 N$. Thus, the inherent P-wave anisotropy $\varepsilon = (A - C)/2C$ equals inherent S-wave anisotropy $\gamma = (N - L)/2 L$. The modulus $\eta = F/(A - 2 L)$ is freely perturbed within the range [0.8,1.1]. This is a narrower range for η than used by Xie *et al*. (2015) (in that work $\eta \in [0.6,1.1]$) in order to eliminate the strike angle ambiguity. Xie *et al*. (2015) found that two groups of models with orthogonal strike directions fit the data equally well, and these two groups of models have similar inherent S-wave anisotropy and dip but different values of η. Therefore, reducing the range of η eliminates this bifurcation and simplifies the resulting models. We discuss the impact of this constraint on the strike angle in Section 5.2. The dip angle θ and strike angle ϕ range between 0° and 90°.

Because Love wave sensitivity is shallower than Rayleigh wave sensitivity (Figs 4c and d) at a given period, the amplitude of inherent S-wave anisotropy γ is poorly determined in the lowermost crust of Tibet. This is illustrated in Fig. 8, which shows the results of three inversions of the same data in Tibet (Point A) but with different constraints on γ: (a) $\gamma \geq 0$ throughout the crust, (b) $\gamma \geq 0$ throughout the crust but $\gamma = 0$ at the base of the crust
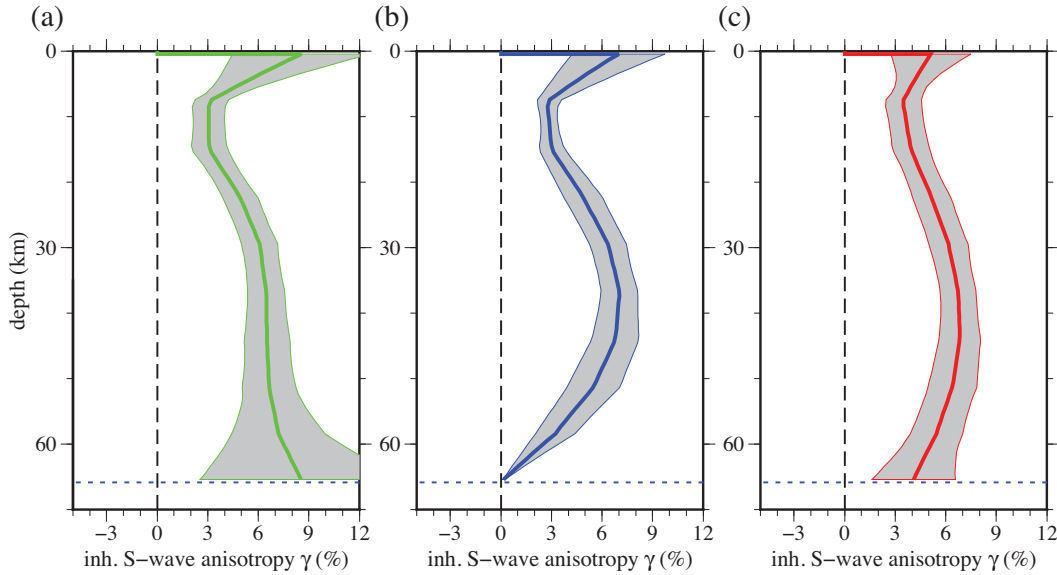
Figure 8. Mean (solid coloured lines) and standard deviation (grey corridors) of posterior distributions of inherent S-wave anisotropy (γ) at Point A in Tibet showing the vertical variation of this quantity with different constraints applied in the inversion: (a) $\gamma \geq 0$ across the crust, (b) $\gamma \geq 0$ across the crust but γ is set to 0 at the base of the crust, similar to Xie *et al.* (2013) and (c) $0 \leq \gamma \leq 10$ per cent across the entire crust as done in this paper. γ is not well constrained by our observations below 50 km depth.

and (c) $0 \leq \gamma \leq 10$ per cent throughout the crust. These constraints produce very different estimates of γ below 50 km depth in the crust. In particular, without a constraint beyond the positivity constraint ($\gamma \geq 0$), the estimate of γ in the lowermost crust of Tibet is unstable. For this reason, we seek a small amplitude model here and apply the constraint that $0 \leq \gamma \leq 10$ per cent throughout the crust across the entire study region. The result of this constraint is that γ will tend to be approximately constant with depth in the lowermost crust of Tibet, as shown in Fig. 8(c).

We have modeled the sediments as isotropic even though Tibet is surrounded by large basins where there is strong evidence of anisotropy. However, because the model of Shen *et al.* (2016) is based exclusively on Rayleigh wave data it does not provide a particularly accurate reference for sedimentary structure, in particular sedimentary thickness. Thus, inferences we might draw here about sedimentary anisotropy would be suspect. In order to constrain the structure of the sediments better, additional data such as receiver functions or the H/V ratio, which are more sensitive to the shallower depths, should be added. We discuss sedimentary anisotropy in Section 6.2.3 where we provide evidence that the sediments are strongly anisotropic, so much so that we are forced to eliminate the amplitude constraint and allow γ in the sediments to be >10 per cent. However, modeling them as isotropic does not affect our primary conclusions, although it does mean that we are not able to fit our data well within the basins.

In terms of the mantle parametrization, the use of hexagonal symmetry with a slow symmetry axis is not common. This is because mantle anisotropy produced by the lattice-preferred orientation (LPO) of olivine is modeled either as hexagonally symmetric with a fast symmetry axis or as orthorhombic, depending on whether the two slower olivine crystal axes scatter randomly or not (Christensen 1984). However, if the mantle anisotropy is caused by partial melt, then mantle anisotropy could be modeled either as hexagonally symmetric with a slow symmetry axis or orthorhombic, depending on the shape of the melt pockets (e.g. Thomsen & Anderson 2015). In any case, because our surface wave observations extend only up to 50 s period, they poorly constrain mantle anisotropy beneath Tibet.

Tests of several different mantle parametrizations and constraints show, however, that changes in the parametrization only affect estimated crustal structures within the estimated uncertainties.

For these reasons, we parametrize mantle anisotropy (Fig. 7) simply in terms of apparent quantities rather than inherent properties, and beneath 200 km the model is set to be AK135 (Kennett *et al.* 1995), which is isotropic. In particular, we describe the mantle as a VHS medium plus additional apparent azimuthal anisotropy. In this case, mantle radial anisotropy decouples from azimuthal anisotropy and both are apparent quantities. We estimate $\hat{V}_{SV}$ as a free parameter in the uppermost mantle, represent it with five B-splines, and allow it to vary within the range $\hat{V}_{SV0} (1 \pm 0.15)$, where the reference value $\hat{V}_{SV0}$ is from Shen *et al.* (2016). We compute $\hat{V}_{SH}$ from $\hat{V}_{SV}$ by assuming a constant value of $\hat{\gamma} = 4.5$ per cent, a value that is consistent with the average of mantle apparent radial anisotropy across the study region determined by Shapiro *et al.* (2004). This is presented in Fig. 7 as $\hat{V}_{SH} = f(\hat{V}_{SV})$, which should be read '$\hat{V}_{SH}$ is a function of $\hat{V}_{SV}$'. We also estimate the apparent amplitude of azimuthal anisotropy $\hat{\Gamma}$ (eq. 7) and the local fast direction $\hat{\varphi}$, both of which are set to be constant with depth in the mantle. We further set $\hat{V}_{PV} = 1.77\hat{V}_{SV}$ and $\hat{V}_{PH} = 1.77\hat{V}_{SH}$, which sets apparent P-wave anisotropy equal to apparent S-wave anisotropy. $\hat{\eta}$ is freely varying within the range [0.8,1.1]. Because we do not infer any inherent properties of the mantle anisotropy we do not show mantle anisotropy in plots of inherent anisotropy. However, plots of apparent anisotropy do include mantle anisotropy. In any event, we will focus our discussion on the crustal part of the model.

5 RESULTS

The Bayesian Monte Carlo inversion is based on the observed data (described in Section 2), the forward computation algorithm (described by Xie *et al.* 2015 in detail), the starting model, and prior information consisting of constraints on the model. As discussed in Section 4, the starting model comes from Shen *et al.* (2016), which is an isotropic V_{sv} model derived exclusively from Rayleigh waves,
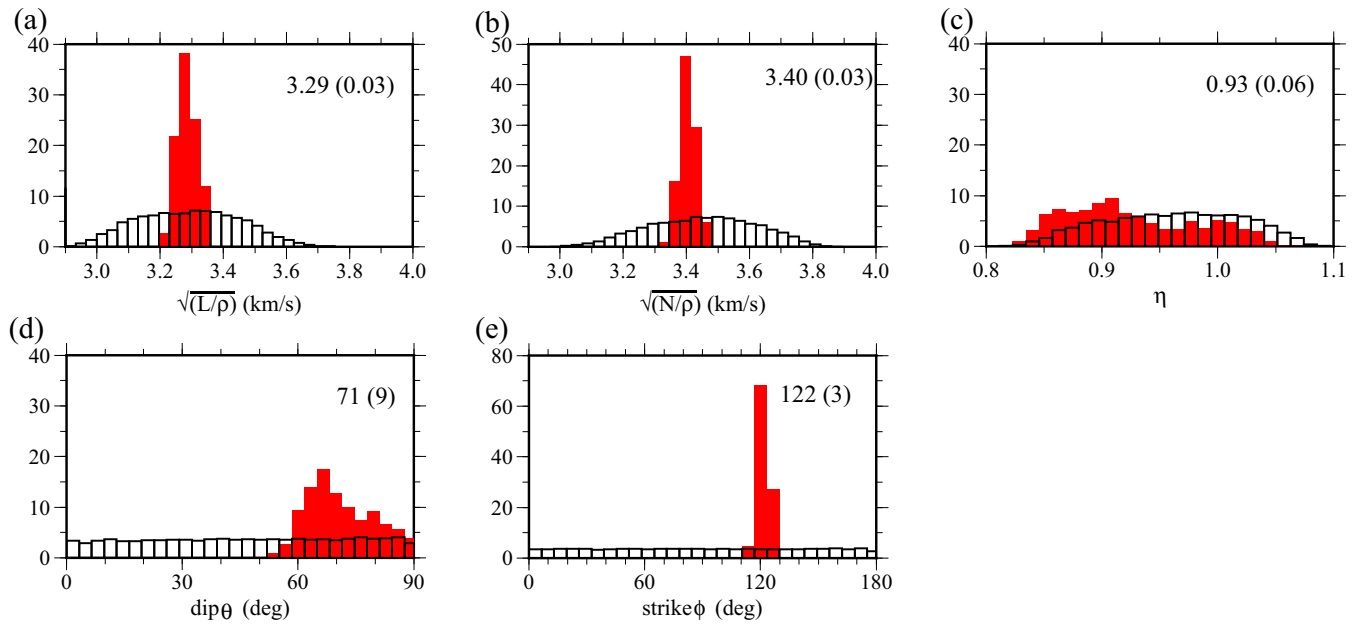
Figure 9. Example comparison of prior and posterior marginal distributions from the Bayesian Monte Carlo inversion for five example model parameters at 10 km depth for Point A in Tibet (Fig. 2a): $\sqrt{L/\rho}$, $\sqrt{N/\rho}$, η, θ and ϕ. White histograms are the prior marginal distributions and red histograms are the posterior marginal distributions. The average and standard deviation of the posterior distributions are presented on each plot.
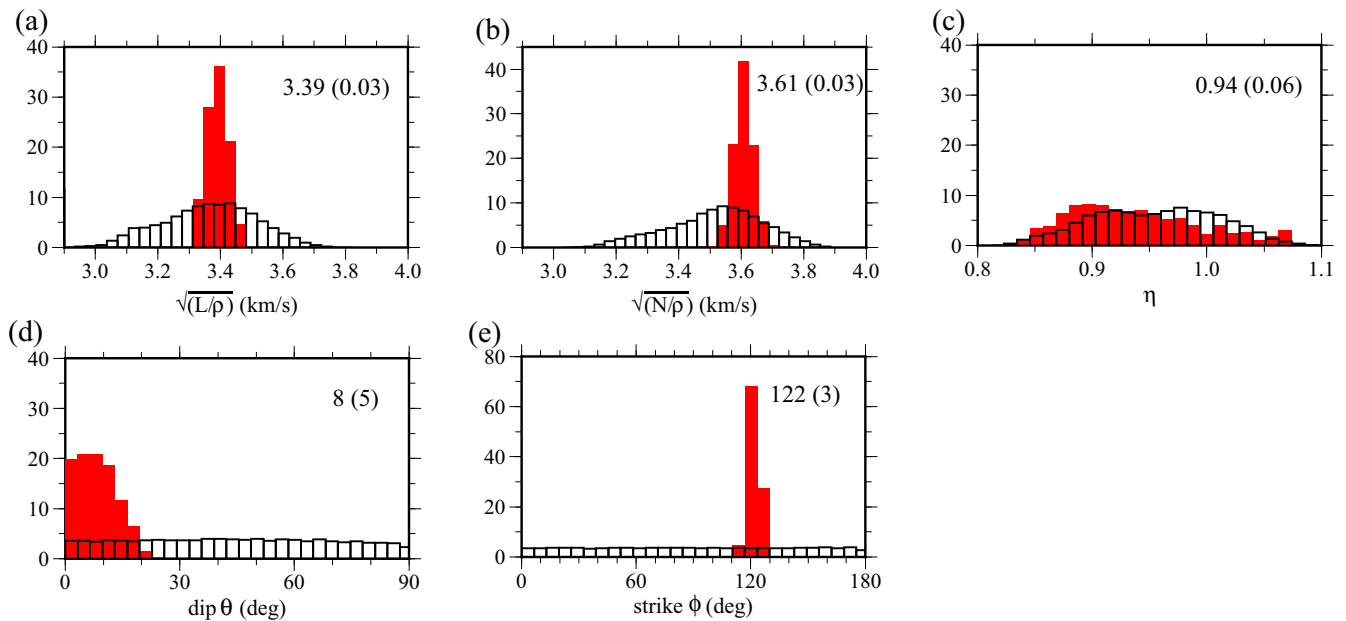

Figure 10. Similar to Fig. 9, but at 30 km depth, again for Point A in Tibet.

and the constraints guide the formation of the prior distribution at each location.

The Bayesian Monte Carlo inversion method is similar to that described in a series of recent papers by Shen *et al.* (2013a,b) and elsewhere (e.g. Shapiro & Ritzwoller 2002; Zheng *et al.* 2011; Yang *et al.* 2012; Zhou *et al.* 2012; Tian *et al.* 2013; Xie *et al.* 2013; Shen *et al.* 2013c, 2016; Deng *et al.* 2015; Kang *et al.* 2015; Shen & Ritzwoller 2016). Here, we invert the data at every location on a $0.5° \times 0.5°$ grid and produce a set of models that define the posterior distribution of models that fit the data accept-

ably. We summarize each posterior distribution by its mean, which we refer to as the 'mean model', and standard deviation, which together define the final model with an estimate of uncertainty at each depth and for each model variable. We present the model here in terms of the inherent elastic tensor and its orientation (dip and strike). A discussion of the apparent anisotropy that results from this representation occurs in Section 6.1. Examples of marginal posterior distributions for selected model characteristics are presented in Figs 9 and 10 for 10 and 30 km depth, respectively, and are discussed further below.
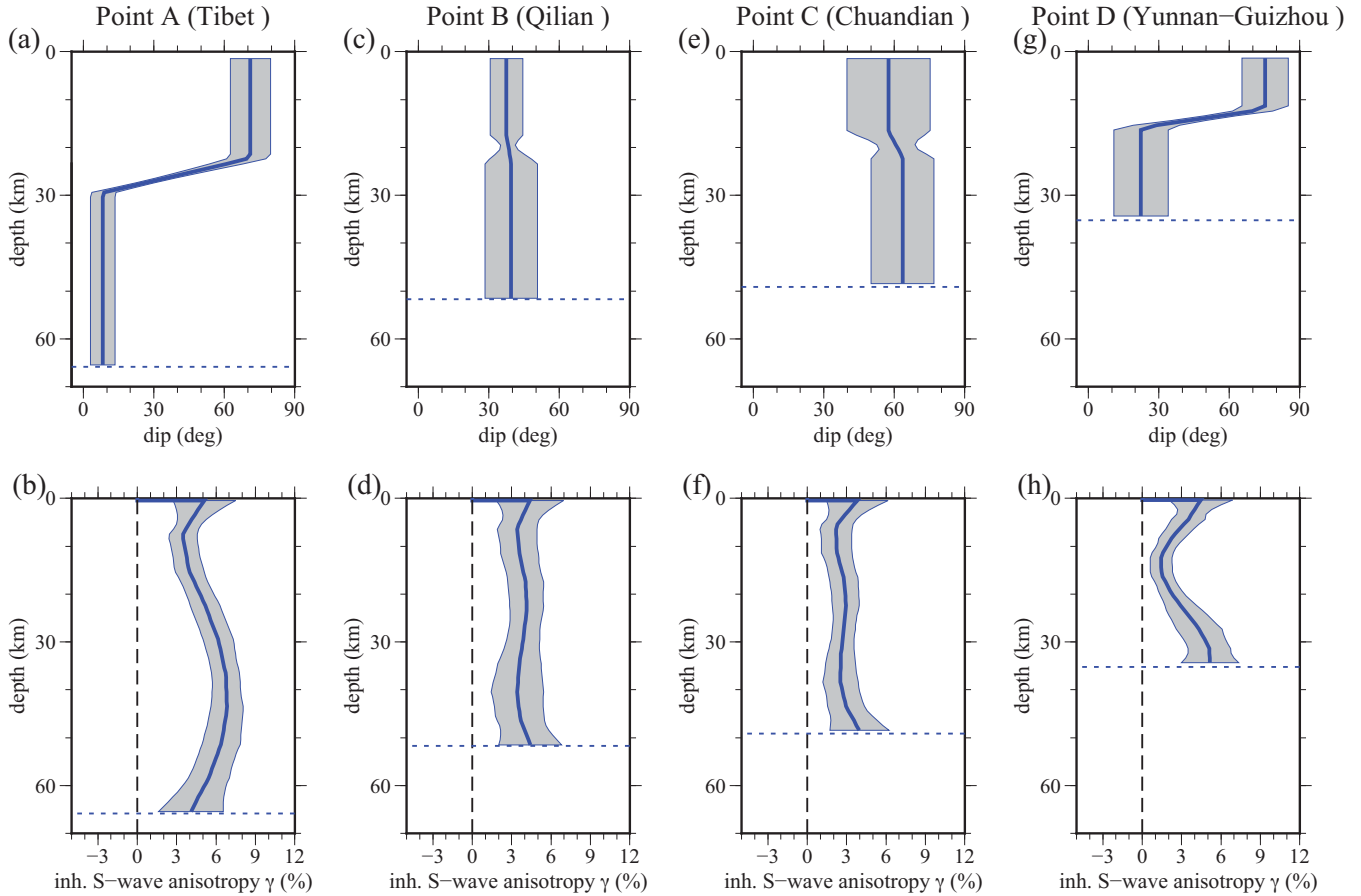
Figure 11. Posterior distributions of inherent anisotropic variables at Points A–D (Fig. 2a) showing (a), (c), (e) and (g) the vertical variation of the dip angle θ and (b), (d), (f) and (h) the inherent S-wave anisotropy γ. The one-standard deviation extent of the posterior distribution is shown at each depth with the grey corridor and the average is plotted with bold black solid lines. Only the crystalline crustal part of the model is shown because sediments are isotropic and the mantle is parametrized in terms of apparent moduli, so no inherent property is inferred.

5.1 Example results at four locations

We first present the results of the inversion of the data presented in Fig. 5 at the four locations identified in Fig. 2(a): Point A in eastern Tibet, Point B in the Qilian terrane north of Tibet, Point C in the central Chuandian terrane just off southeastern edge of the Tibetan plateau and Point D in the Yunnan-Guizhou plateau.

5.1.1 Example result at Point A

At Point A, the Love–Rayleigh phase velocity difference increases with period, while the amplitude of Rayleigh wave azimuthal anisotropy decreases with period (Figs 5a–c). Figs 5(a)–(c) show that the data are fit well (red lines) by the mean model with the parametrization that allows two different dip angles in the crust. The fit delivered by the mean models produced from inversions with two other parametrizations are also shown in Figs 5(a)–(c): an isotropic model (green lines) and a model with a constant dip angle throughout the crust (black lines, 1-dip). Neither of these models can fit the Love wave and Rayleigh wave phase speeds simultaneously across most of Tibet. This provides the primary justification for the introduction of the discontinuity in dip angle in the middle crust in our parametrization.

Aspects of the posterior distributions at Point A are presented in Figs 9 and 10, which display marginal distributions for inherent $\sqrt{L/\rho}$, $\sqrt{N/\rho}$, η, dip angle θ and strike angle ϕ at depths

of 10 and 30 km. These are five of the seven parameters that describe the elastic tensor and its orientation at each depth. The other two (compressional moduli A and C) are scaled from the shear moduli L and N and are, therefore, not shown. At both depths L and N are well constrained; the standard deviations of the posterior distributions are less than about 1 per cent at both 10 and 30 km depth. The strike angle is constant in the crust and is also well constrained, with a standard deviation of about $3°$. In contrast, η is not well constrained at either depth, which tends to be true across the study region. The most notable difference between the two depths is the very different dip angle at 10 km ($71° \pm 9°$) compared with 30 km ($8° \pm 5°$). The foliation plane dips steeply in the upper crust and is subhorizontal in the lower crust at this location in eastern Tibet, and across most of Tibet, as we will show. In the lower crust here, the foliation plane is observationally indistinguishable from horizontal (i.e. the symmetry axis is indistinguishable from vertical).

This information can be viewed in a different way in Fig. 11 in which one standard deviation bounds around the mean of the posterior distribution are presented as a function of depth for the dip angle and inherent S-wave anisotropy, γ (eq. 5). The change in the dip angle with crustal depth is shown for Point A in Tibet in Fig. 11(a) and γ is seen in Fig. 11(b) to range from 3 to 5 per cent in the uppermost crust (depth <10 km), to about 7 per cent at 40 km depth, and then decrease with depth to ∼4–5 per cent in the lowermost crust.

5.1.2 Example result at Point B

At Point B, which is located in the Qilian terrane just north of Tibet, the isotropic model also does not fit the data (Figs 5d–f), thus crustal anisotropy is also required outside of Tibet. However, the data can be fit either with a model in which we allow the dip angle to change in the middle crust or a model where we constrain the dip angle to be constant throughout the crust. The reason for this is seen in Fig. 11(c), which shows that the dip angle is essentially indistinguishable between the upper and lower crust at this location ($\sim$40°). Fig. 11(d) shows that γ is approximately constant with depth, averaging about 4 per cent across the crust at this location.

5.1.3 Example result at Point C

At Point C, the data differ from those at both Points A and B in that the Love–Rayleigh phase speed difference can nearly be fit with an isotropic model (Fig. 5g; indicating near-zero apparent radial anisotropy). However, the high amplitude of azimuthal anisotropy guarantees the existence of crustal anisotropy. Similar to Point B, the dip angle ($\sim$60°) at Point C does not change strongly with depth across the crust (Fig. 11e), but the dip angle is steeper than at Point B. The amplitude of inherent *S*-wave anisotropy γ averages between 2 and 3 per cent across most of the crust (Fig. 11f), which is weaker than at Points A and B.

5.1.4 Example result at Point D

Crustal anisotropy at Point D is more similar to Tibet in that two dip angles are needed to fit the data shown in Figs 5(j)–(l). Although the dip angle (Fig. 11g) in the upper crust is similar to that in Tibet (>70°), the dip angle in the lower crust is larger ($\sim$20°) and is distinguishable from zero. Thus, the lower crustal foliation plane in the Yunnan-Guizhou plateau is not as horizontal as beneath Tibet, but is shallowly dipping. Also, the vertical distribution of inherent *S*-wave anisotropy at Point D (Fig. 11h) differs from Tibet. The anisotropy in Tibet is strong throughout the crust, whereas beneath the Yunnan-Guizhou plateau it is concentrated in the uppermost ($\sim$4 per cent) and lowermost crust ($\sim$5 per cent) with a minimum at a depth of about 15 km ($\sim$1.5 per cent).

In Section 6.1, we discuss the apparent crustal anisotropy computed from the inherent anisotropy and dip angle discussed here, as well as apparent mantle anisotropy.

5.2 Results across the entire region: mean of the posterior distribution

Aspects of the resulting model (dip angle θ, inherent *S* wave anisotropy γ), defined as the mean of the posterior distribution at each depth, are shown in Fig. 12 at depths of 10 and 30 km in the crust. These depths bracket the discontinuity in dip angle across the entire study region. The estimated strike of anisotropy, which is constant with depth within the crust, is shown in Fig. 13(a) in which the orientation of the bars indicates the strike orientation (ϕ). As described in Section 4, we have deliberately narrowed the allowed range of η considered; thus our resulting models approximately possess so-called elliptical anisotropy (e.g. Thomsen 1986; Xie *et al.* 2015). As a consequence, the crustal strike orientation generally follows the Rayleigh wave fast-axis orientation at short periods (Fig. 3c). However, as discussed by Xie *et al.* (2015), if η is allowed to vary broadly enough there will be two subsets of models

in the posterior distribution with orthogonal strike angles. We circumvented this bimodality by constraining η to be relatively large. Nevertheless, at each location, there is another strike orientation that is consistent with our data, which we also show in Fig. 13(b). We note that if the dip angle is small so that the foliation plane is nearly horizontal, the strike angle loses its significance.

At 10 km depth (Figs 12a and b), the foliation plane in the upper crust is steeply dipping across most of the study region, including the Tibetan plateau and its surroundings. In contrast, the Qaidam basin, Ordos block, southern Tibet and the Sichuan basin are characterized by shallow dip angles in the shallow crust. The inherent *S*-wave anisotropy (Fig. 12b) ranges from $\sim$2 to $\sim$6 per cent across most of the study region. Inherent *S*-wave anisotropy in the shallow crust is not notably stronger in Tibet than in surrounding areas. Because the sediments in the model are isotropic, anisotropy in the sediments may bias γ to larger values at 10 km depth beneath the deep sediments of the Sichuan and Qaidam basins.

At 30 km depth (Figs 12c and d), the interior of eastern Tibet has a subhorizontal foliation plane that is largely indistinguishable from a VHS medium. Near the boundaries of the Tibetan plateau, particularly between Tibet and the western Yangtze craton (including the Sichuan Basin) and in the Qilian terrane north of Tibet, the anisotropy attributes of the medium are moderately to steeply dipping in the middle-to-lower crust (Fig. 12c). The inherent *S*-wave anisotropy (Fig. 12d) is relatively large across the entire region of study with amplitudes ranging from about 3–6 per cent. The strongest inherent *S*-wave radial anisotropy is observed in the interior of eastern Tibet and in the Yunnan-Guizhou plateau south of the Sichuan basin. Weaker inherent *S*-wave anisotropy is observed near the eastern boundary of the Tibetan plateau and in the Sichuan basin and Ordos block. At most places, γ grows with depth from 10 to 30 km in the crust but not beneath the major basins.

For a more complete view of crustal anisotropy, two vertical profiles of crustal inherent *S*-wave anisotropy and dip angle are presented in Fig. 14. The locations of the two profiles are shown in Fig. 2(b). Profile A starts just north of the Kunlun fault east of the Qaidam basin, runs through the Songpan-Ganzi terrane of eastern Tibet and the Chuandian terrane, off the southeastern margin of Tibet, and into the Yunnan-Guizhou plateau. Profile B runs from the boundary between the Lhasa and Qiantang terranes in eastern Tibet, through the Qiantang and Songpan-Ganzi terranes, and northeast off the Tibetan plateau to terminate just within the Ordos block. Figs 14(a) and (b) present the dip angles along these profiles in two ways: colour-coded and also with orientation bars that lie along the foliation plane at 50 km lateral intervals. The vertical bifurcation of the dip angle between the steeply dipping upper and shallowly dipping lower crust is the most striking feature of both profiles. The principal exception occurs near the southeastern border of Tibet where steeply dipping anisotropy appears throughout the entire crust (Fig. 14a). Figs 14(c) and (d) present inherent *S*-wave anisotropy (γ) and illustrate that along these profiles γ tends to grow with depth in the crust. In general, γ is more homogeneous laterally than vertically, although it is smaller beneath the Ordos block than elsewhere along these profiles. As discussed earlier, γ is poorly estimated below 50 km depth.

Because the lower crustal dip angle is small throughout most of the study region, the strike angle for the lower crust has little significance. This may be one of the reasons why a single strike angle at each location across the crust suffices to fit the data in Tibet. As discussed in Section 6.1, this is related to the fact that there is very low amplitude apparent azimuthal anisotropy in the lower crust of Tibet.
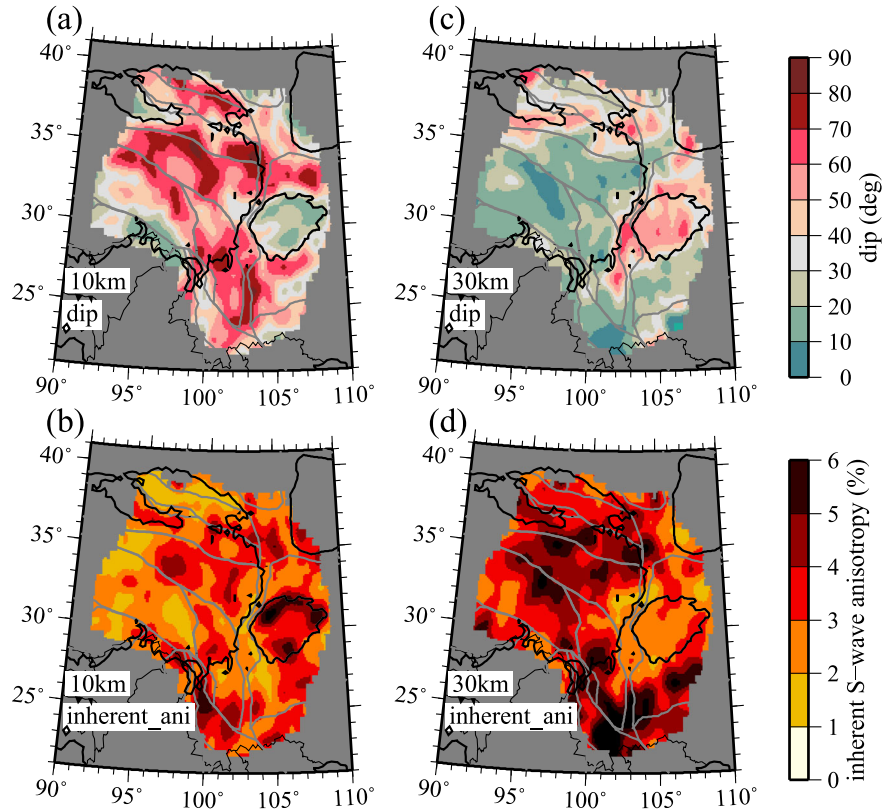
Figure 12. Map views of the dip angle θ and inherent S-wave anisotropy γ, respectively, at depths of: (a) and (b) 10 km and (c) and (d) 30 km.
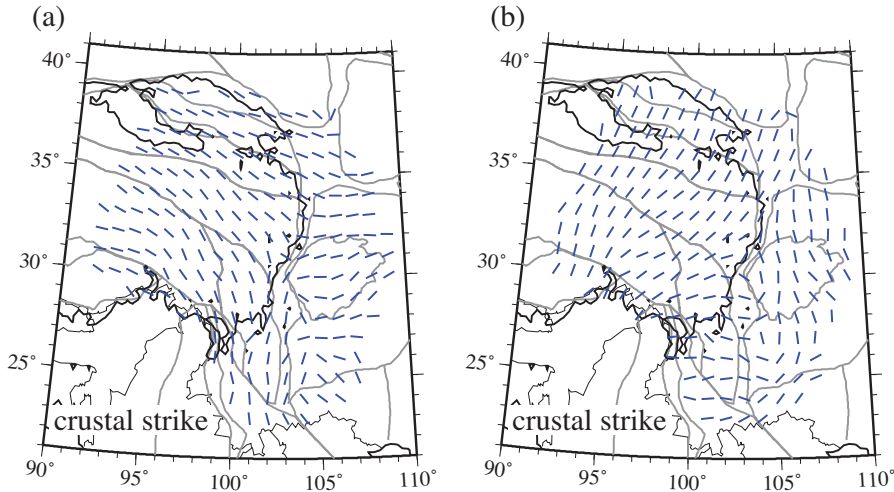

Figure 13. (a) The orientation of the local crustal strike angle ϕ determined here, which is constant vertically throughout the crust, is shown with blue bars. (b) Crustal strike orientation perpendicular to the results shown in (a), acknowledging the ambiguity in the estimate of the crustal strike angle.

Discussion of the interpretation of these results is delayed until Section 6.2. Comparison with apparent radial and azimuthal anisotropy, which are the more commonly estimated quantities in surface wave studies, is found in Section 6.1. We also show γ at 5 km above Moho in Section 6.3.1 while discussing the vertical distribution of the amplitude of inherent anisotropy.

5.3 Data misfit

The misfit to the data (Rayleigh wave phase speeds, Love wave phase speeds, amplitude and fast-axis directions of Rayleigh wave azimuthal anisotropy) is presented as the square root of the reduced chi-squared misfit in Fig. 15. Specifically, misfit is defined as follows. For model m, let $S(m)$ be the reduced chi-square:

$$S(m) = \frac{1}{N} \sum_{i=1}^{N} \frac{(D(m)_i - D_i)^2}{\sigma_i^2} \tag{8}$$

where D_i is the observation of datum i, $D(m)_i$ is that datum predicted from model m, σ_i is the standard deviation of datum i and N is the total number of observations. The error bars in Fig. 5 illustrate the nature and number of the observations and their standard deviations. The misfit presented in Fig. 15 is the square root of $S(m)$ across the study region. A value of unity would indicate that the data are fit on
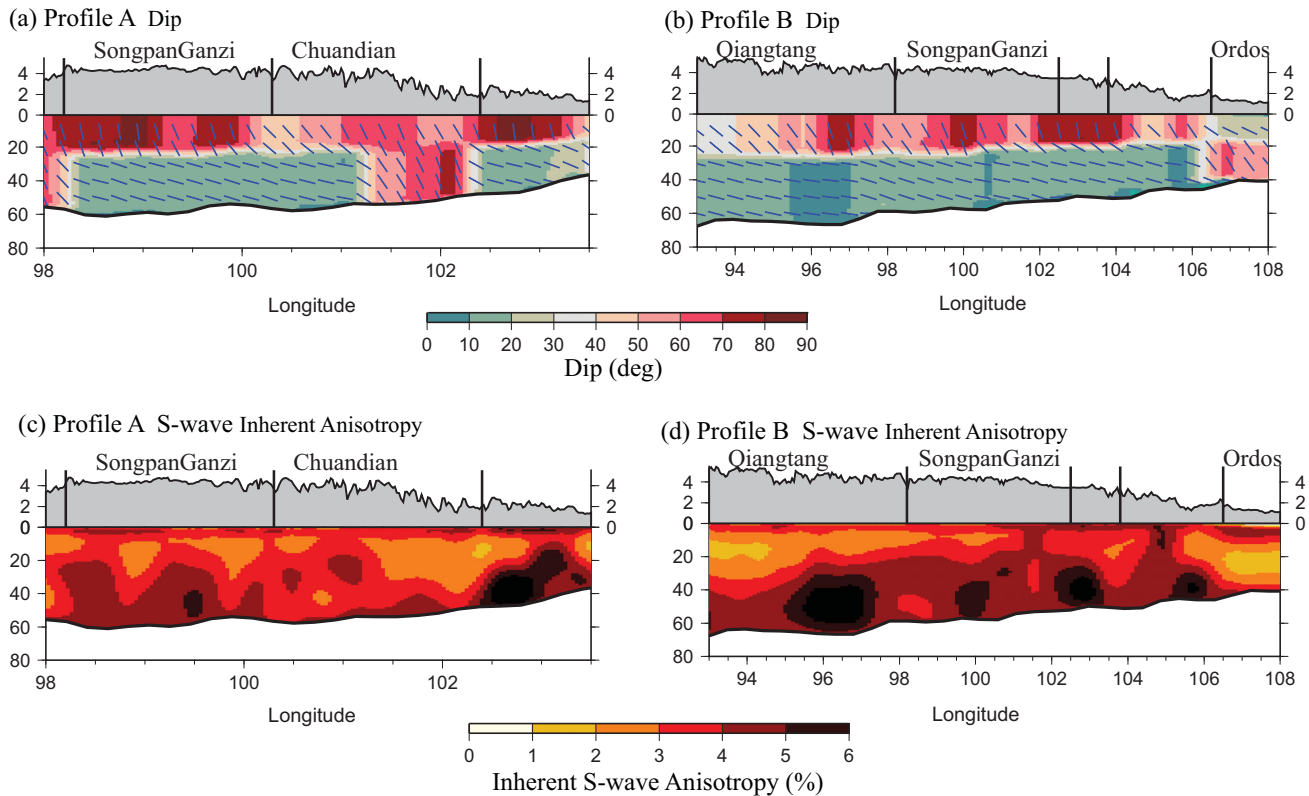
Figure 14. Vertical transects of inherent *S*-wave anisotropy γ and dip angle θ along profiles A and B identified in Fig. 2(b). In (a) and (b) dip angle is colour-coded and the orientation of the foliation plane of anisotropy is presented with short blue bars. Horizontally, centres of the blue bars are 50 km away from each other, and vertically the spacing is 10 km. The dip angle is what geologists refer to as 'true' rather than the 'apparent' dip projected along the profile. In (c) and (d), γ is colour-coded in percent. Only the crustal part of the model is presented because the mantle is parametrized in terms of apparent moduli.
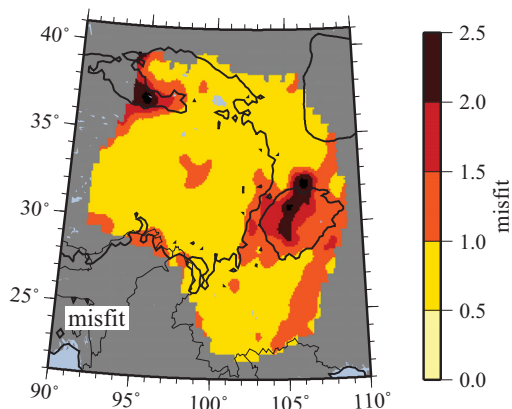
Figure 15. Geographic variation in data misfit produced by the best-fitting model at each location. Misfit is defined as the square root of the reduced chi-squared value at each location (eq. 8).

average at the level of one standard deviation. The data across most of the region are fit at a level better than 1.5 standard deviations, with the exception of the large sedimentary basins (Sichuan, Qaidam). To fit the data in the basins we would need to introduce anisotropy to the sediments, which would complicate the inversion and is beyond the scope of this paper.

5.4 Results across the entire region: standard deviation of the posterior distribution

As discussed by Shen & Ritzwoller (2016), it is not entirely straightforward to use the posterior distribution to quantify model uncer-

tainty. They argue that the standard deviation of the posterior distribution does not provide an estimate of the effect of systematic errors and provides an overestimate of the effect of non-systematic errors. They go on to quantify non-systematic errors in several different ways and argue that the standard deviation of the posterior distribution overestimates the effect of non-systematic errors by about a factor of 4. Here, we present the standard deviation of the posterior distribution to guide the use of the model and refer to it as model uncertainty, but it should be understood that this uncertainty does not include potential systematic contributions and is a very conservative estimate of non-systematic error.

The standard deviation of the posterior distribution (uncertainty) is shown in Fig. 16 at depths of 10 and 30 km for dip angle and inherent *S*-wave anisotropy γ. The uncertainty for dip lies between 5° and 15° at both 10 and 30 km depths in most regions other than the Sichuan and Qaidam basins (Figs 16a and b). (The uncertainty beneath the basins is magnified because the data cannot be fit as well there due to the fact that we have not included anisotropy in the sediments.) In contrast, as shown in Fig. 16(e), the standard deviation of the posterior distribution for the strike angle is smaller, averaging about 7° outside the basins, but is larger near the periphery of our study region where the fast-axis directions of Rayleigh waves are less well constrained. One reason the strike uncertainty is smaller than the dip uncertainty is because the strike angle is constrained to be constant within the crust, whereas the dip angle is allowed to change within the crust. A second reason is that strike is constrained in a direct way by observations of the Rayleigh wave fast azimuth, whereas the dip angle trades off with the inherent elastic moduli and together they are less directly constrained by our observations. The average value of 7° is close to the uncertainty
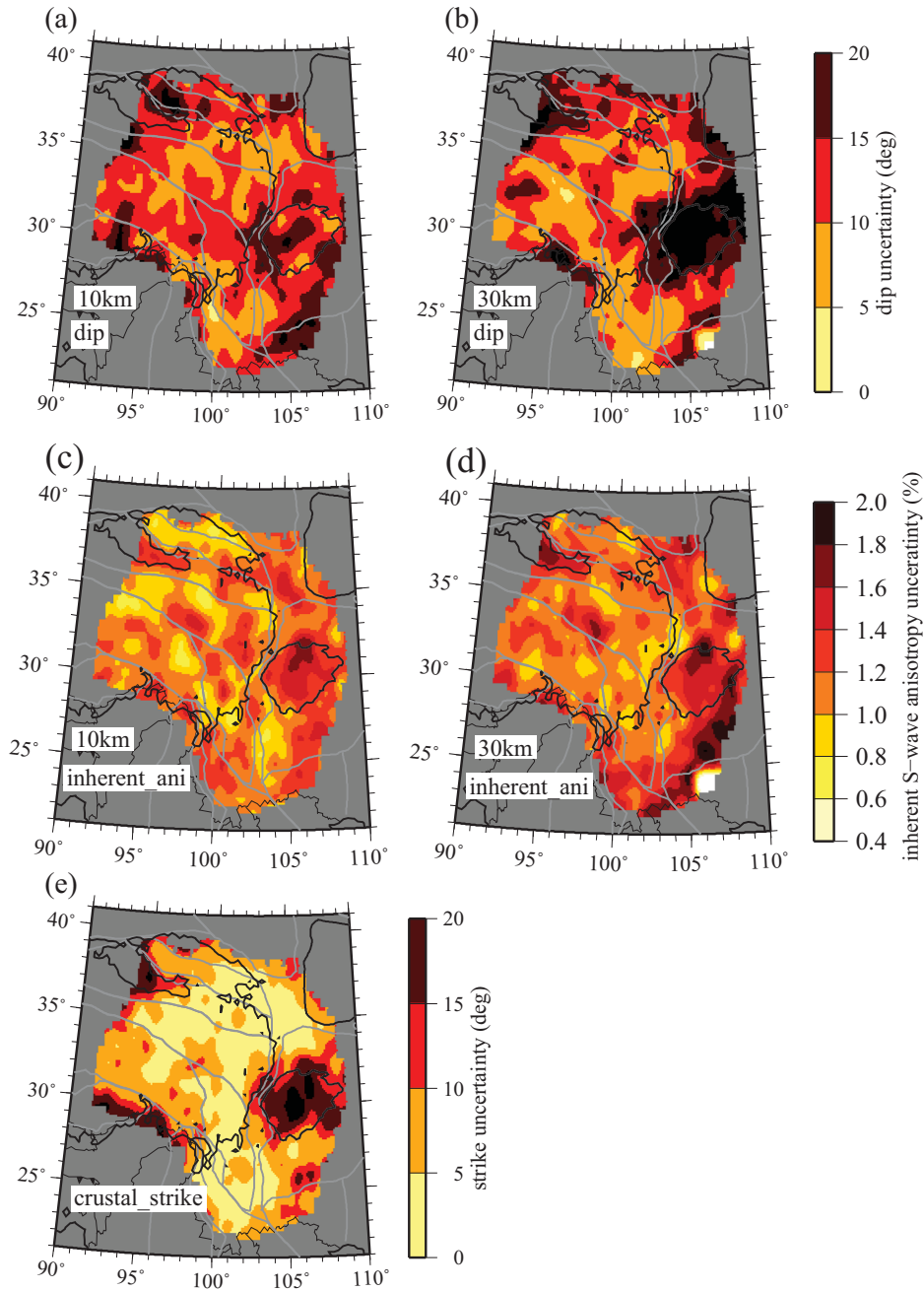
Figure 16. Map views of the standard deviation of the posterior distribution for (a) and (b) dip angle θ and (c) and (d) inherent *S*-wave anisotropy γ at depths of 10 and 30 km, respectively. (e) Standard deviation of the posterior distribution for strike angle, which is constant in the crust.

for Rayleigh wave fast azimuth at short periods (e.g. Figs 5c, f, i and l).

The average uncertainty for inherent *S*-wave anisotropy (γ) is about 1.2 per cent at 10 km depth and slightly larger at 30 km depth (Figs 16c and d). At both depths, the uncertainty is larger outside of Tibet. At 30 km depth, the uncertainty is extremely large in the southeastern part of the study region. This is because uncertainty grows near to the Moho due to trade-offs across the interface. The Moho lies between 35 and 40 km where large uncertainties exist in γ. The estimated uncertainty in γ at 5 km above Moho is shown and discussed in Section 6.3.1. Formally, it is larger at this depth than shallower in the crust but the result we show later actually underestimates uncertainty below 50 km depth because it reflects

the weak anisotropy constraint ($\gamma \leq 10$ per cent), which stabilizes the inversion below a depth of 50 km and reduces the uncertainty estimate.

6 DISCUSSION

6.1 Model presented in terms of apparent anisotropy

In Section 5, we present the estimated THS model in terms of the mean of the posterior distribution of the inherent elastic moduli and orientation at each depth. Particular emphasis is placed on the inherent *S*-wave anisotropy γ (eq. 5) and the dip and strike angles (θ, ϕ) that describe the orientation of the medium's anisotropy
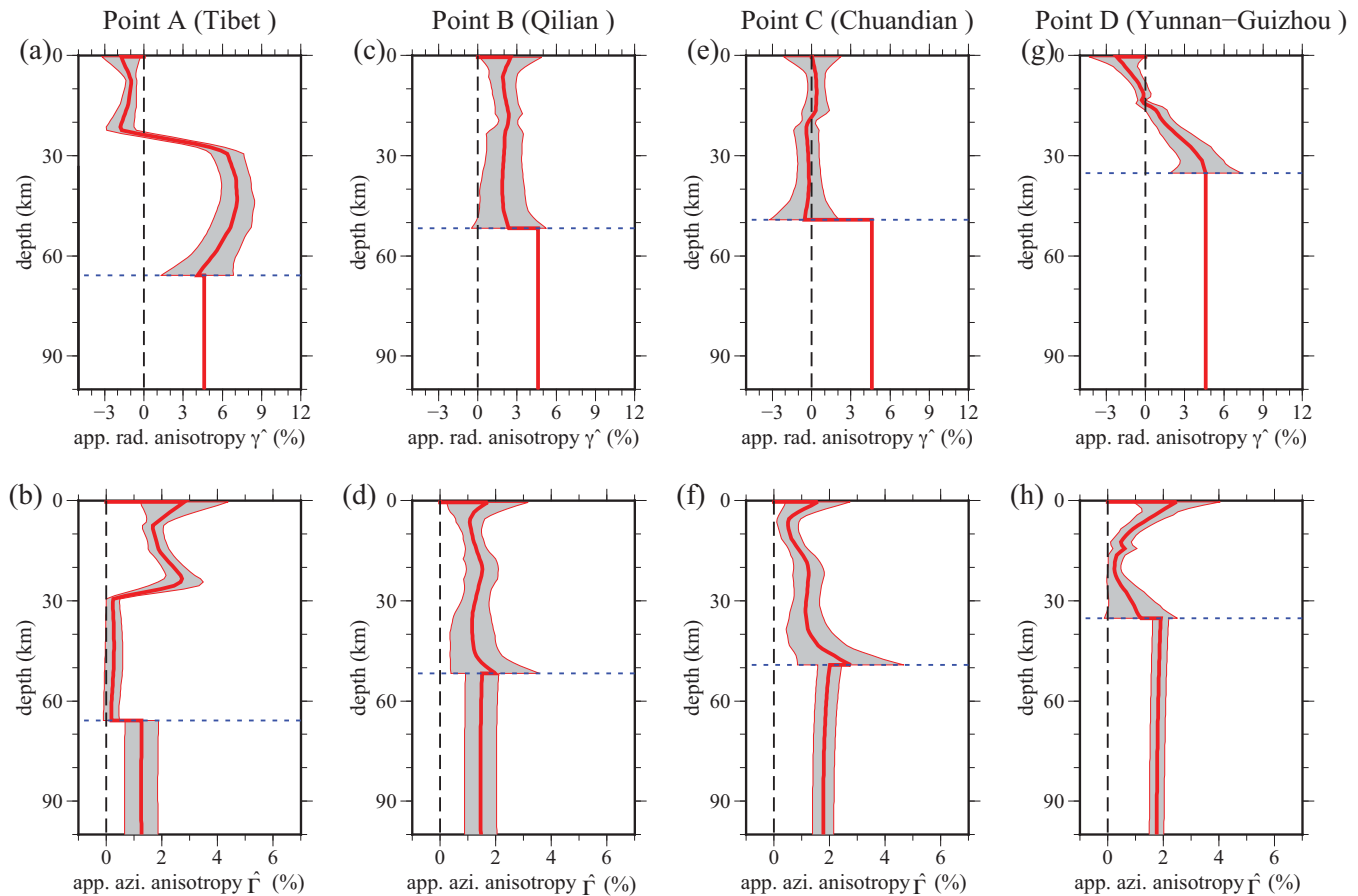
Figure 17. Posterior distributions of apparent radial ($\hat{\gamma}$) and apparent azimuthal ($\hat{\Gamma}$) anisotropy defined similarly to Fig. 11 for comparison.

attributes because these are the variables that are best constrained by surface wave data. The inherent representation of anisotropy presents the elastic tensor in the coordinate frame of the medium as shown in Fig. 1. In the medium frame, the 3-axis of the coordinate system aligns with the symmetry axis of the medium and there is no azimuthal anisotropy. However, in the coordinate system of observation the 3-axis lies normal to the Earth's surface and observations of anisotropy depend on how components of the elastic tensor are affected by the tilt of the medium. When a hexagonally symmetric medium is tilted, both apparent *S*-wave radial anisotropy ($\hat{\gamma}$, eq. 6) and apparent *SV*-wave azimuthal anisotropy ($\hat{\Gamma}$, eq. 7) may be observed. Indeed, most studies of anisotropy using surface waves have described anisotropy in terms of $\hat{\gamma}$ (e.g. Shapiro *et al.* 2004; Panning & Romanowicz 2006; Marone *et al.* 2007; Nettles & Dziewoński 2008; Duret *et al.* 2010; Huang *et al.* 2010; Moschetti *et al.* 2010; Yuan *et al.* 2011; Xie *et al.* 2013; French & Romanowicz 2014) or $\hat{\Gamma}$ (e.g. Simons *et al.* 2002; Marone & Romanowicz 2007; Yao *et al.* 2010; Lin *et al.* 2011; Yuan *et al.* 2011; Pandey *et al.* 2015). As discussed by Xie *et al.* (2015), the apparent values can be computed from the inherent values. In order to aid comparison with other studies, we summarize here the apparent *S*-wave radial anisotropy and apparent azimuthal anisotropy computed from the estimated inherent elastic tensor and its orientation.

Fig. 17 presents results for crustal apparent radial anisotropy $\hat{\gamma}$ and apparent azimuthal $\hat{\Gamma}$ anisotropy at the same locations shown for inherent *S*-wave anisotropy γ and dip angle θ in Fig. 11. Fig. 17 also presents results for $\hat{\gamma}$ and $\hat{\Gamma}$ in the mantle because we parametrize the mantle in terms of apparent quantities. Mantle apparent radial anisotropy $\hat{\gamma}$ is set to 4.5 per cent at all locations, although $\hat{V}_{SV}$ and apparent azimuthal anisotropy $\hat{\Gamma}$ change spatially.

Apparent radial anisotropy is qualitatively similar in the crust at Points A and D (Figs 17a and g), being weakly negative in the upper crust and more strongly positive in the lower crust. $\hat{\gamma}$ attains a maximum value of about 7 per cent at about 45 km depth at Point A and is negative (-1.5 per cent) in the upper crust. Because the foliation plane of the lower crust is subhorizontal across most of Tibet, inherent *S*-wave anisotropy γ and apparent radial anisotropy $\hat{\gamma}$ in the lower crust are very similar at Point A (Figs 11b and 17a). Also at Points A and D, apparent azimuthal anisotropy $\hat{\Gamma}$ dominantly arises from the upper crust. Apparent azimuthal anisotropy is indistinguishable from zero in the Tibetan lower crust (Fig. 17b), thus the lower crustal strike angle has little significance.

At Points B and C, $\hat{\gamma}$ is approximately constant in the crust. At Point C, it is indistinguishable from zero even although the inherent anisotropy γ averages about 3 per cent. This is caused by a dip angle of about 60° across the entire crust, a value that lies near the zero-crossing of anisotropy shown in Fig. 6. $\hat{\Gamma}$ also is approximately constant with depth in the crust at Points B and C.

Mantle apparent radial anisotropy (4.5 per cent) tends to be stronger than crustal radial anisotropy except at Point A in Tibet where lower crustal $\hat{\gamma}$ reaches 7 per cent. At Point A in Tibet, upper crustal apparent azimuthal anisotropy (2−3 per cent) is stronger than mantle apparent azimuthal anisotropy (∼1.2 per cent).

Horizontal slices at depths of 10 and 30 km are presented for the apparent quantities $\hat{\gamma}$ and $\hat{\Gamma}$ in Fig. 18, to contrast with the
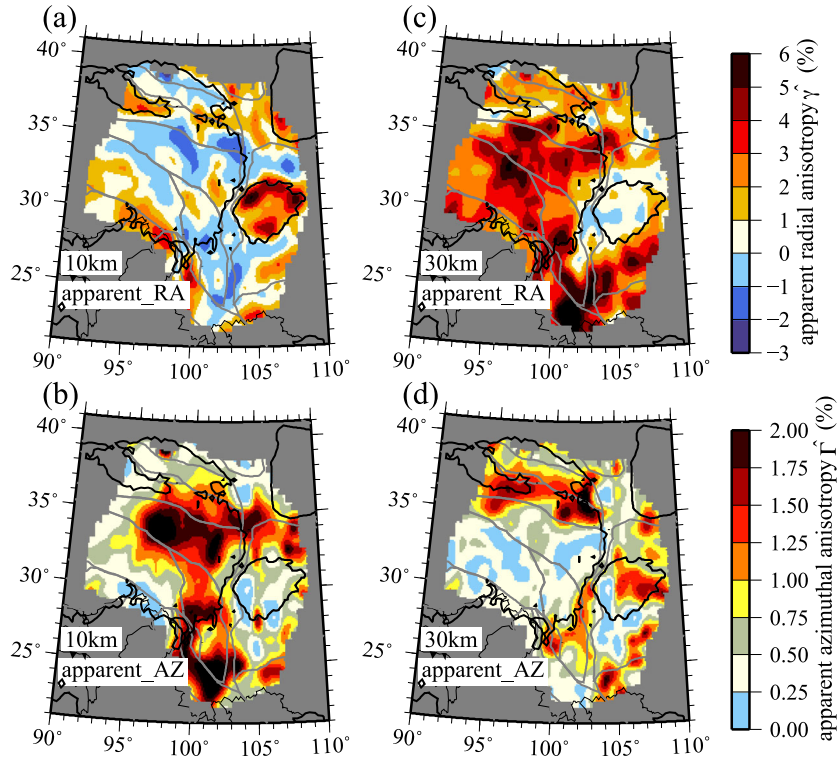
Figure 18. Map views of apparent radial ($\hat{\gamma}$) and apparent azimuthal ($\hat{\Gamma}$) anisotropy defined similarly to Fig. 12 for comparison.
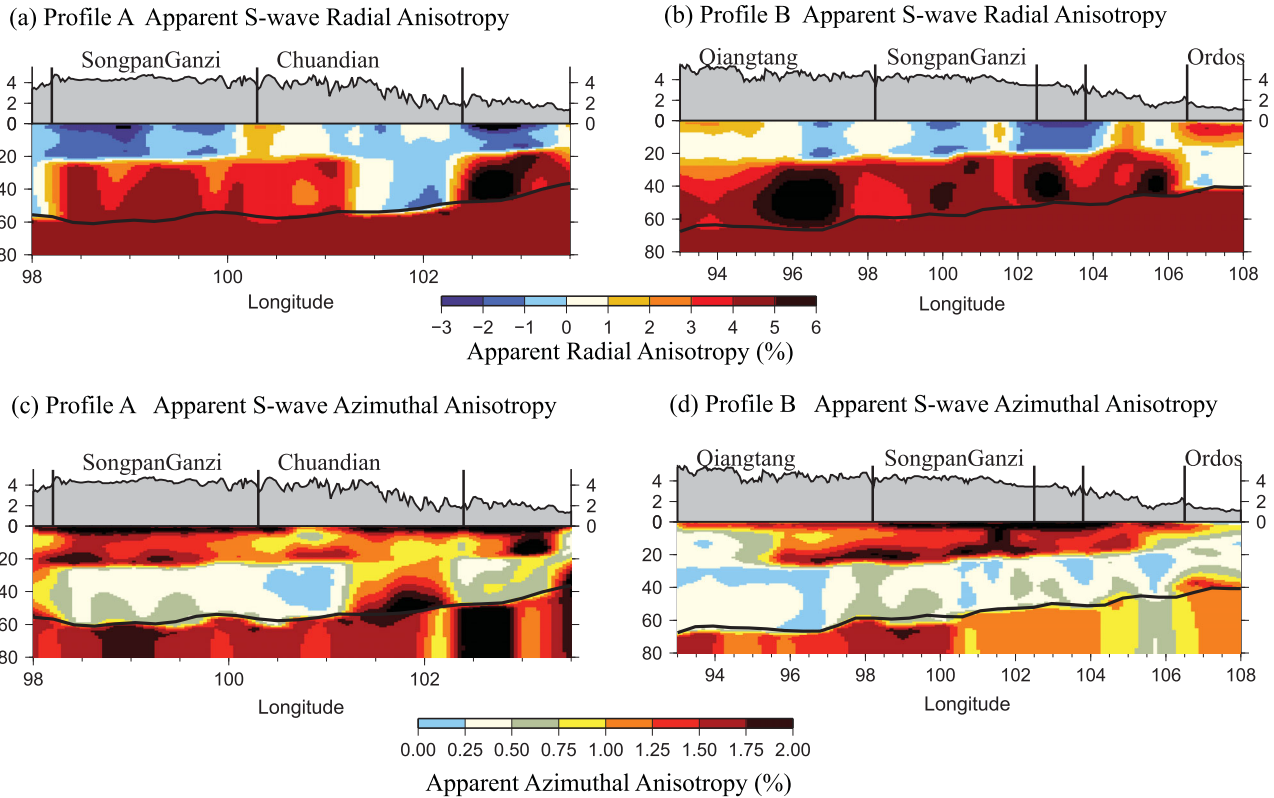

Figure 19. Vertical transects of apparent radial ($\hat{\gamma}$) and apparent azimuthal ($\hat{\Gamma}$) anisotropy defined similarly to Fig. 14 for comparison.

inherent quantities γ and θ found in Fig. 12. Negative $\hat{\gamma}$ commonly coincides with large $\hat{\Gamma}$ in the shallow crust, again due to large dip angle and is explained by Fig. 6. Similarly, in the deep crust large $\hat{\gamma}$ coincides with small $\hat{\Gamma}$ due to a shallow dip angle. Finally, vertical

transects of the apparent quantities $\hat{\gamma}$ and $\hat{\Gamma}$ are presented in Fig. 19 for comparison with the inherent quantities plotted in Fig. 14.

Compared with inherent *S*-wave anisotropy γ, the apparent radial anisotropy $\hat{\gamma}$ (Figs 18a and c; and 19a and b) displays much stronger
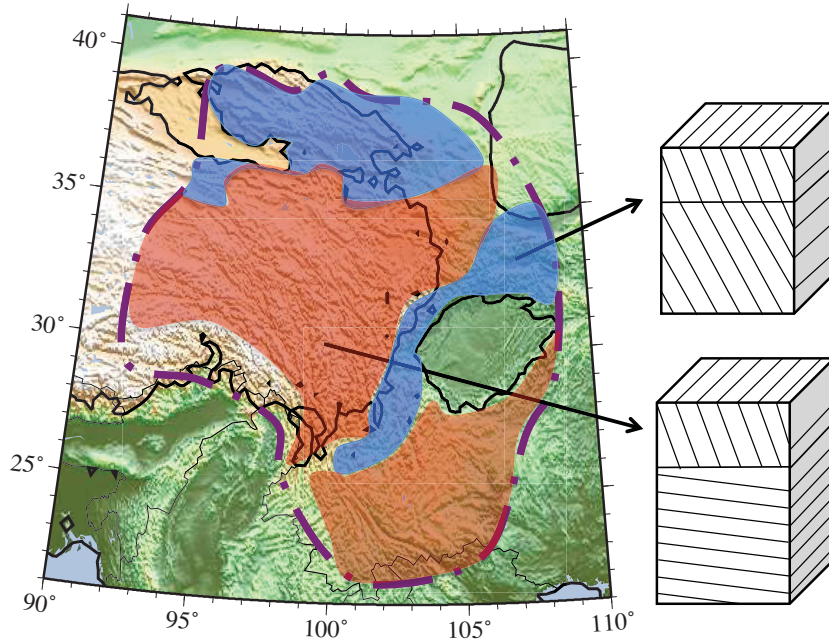
Figure 20. Regionalization of anisotropy in the final 3-D model. The dashed line indicates the study region. The blue shaded regions are characterized by moderately to steeply dipping foliations throughout the entire crust. The red shaded regions have foliations dipping steeply in the upper crust overlying a subhorizontally foliated middle-to-lower crust.

lateral variations because it reflects variations in dip angle in addition to inherent anisotropy. The steep dip angle in the upper crust (Fig. 12a) produces negative apparent radial anisotropy (apparent V_{SH} < apparent V_{SV}) across much of the study region (e.g. Fig. 18a), with the principal exceptions occurring beneath large sedimentary basins. Fig. 19 shows that the negative apparent anisotropy in the upper crust extends beneath much of both vertical profiles. Such negative $\hat{\gamma}$ values were observed across parts of Tibet by Xie *et al.* (2013), who interpreted them as evidence for steeply dipping fractures or faults in the shallow Tibetan crust. Due to the shallow lower crustal dip angles across much of the study region, γ and $\hat{\gamma}$ are similar in the lower crust. Thus across much of the region, Fig. 12(d) is similar to Fig. 18(c), with the notable exceptions being in regions with steep lower crustal dip angles such as the regions flanking Tibet. Profile A in Fig. 19(a) illustrates one of these exceptions (longitudes between 101.3° and 102.5°) and shows that negative apparent radial anisotropy extends throughout the crust in the central-to-southern part of the Chuandian terrane near the southeast border of Tibet.

Azimuthal anisotropy is not an inherent property of a hexagonally symmetric elastic tensor, but reflects the directional dependence of Rayleigh wave speeds that results from the amplitude of inherent anisotropy and the tilting of the medium. When the dip angle is small, as it is across much of the lower crust of Tibet (Fig. 12c), the apparent azimuthal anisotropy is minimal (Fig. 18d). In contrast, lower crustal apparent azimuthal anisotropy (Fig. 18a) is particularly strong near the periphery of Tibet where the lower crustal dip angle is steep. Unlike the lower crust, the anisotropic properties of the upper crust are steeply dipping across much of the study region, so upper crustal apparent azimuthal anisotropy is also strong across most of the region (Fig. 18b). Apparent azimuthal anisotropy, being strong in the upper crust and weak in the lower crust at most locations, is seen clearly in the two vertical profiles in Figs 19(c) and (d).

In summary, there is a vertical dichotomy between crustal apparent azimuthal $\hat{\Gamma}$ and radial $\hat{\gamma}$ anisotropy in most of the study region. Apparent azimuthal anisotropy is strong principally in the upper crust whereas apparent radial anisotropy is strong mostly in the lower crust. The principal exception to this dichotomy lies predominantly near the periphery of Tibet, where the dip angle is nearly constant throughout the crust.

6.2 Geological and physical significance

6.2.1 Regionalization

The results presented here illustrate that the inferred crustal anisotropy is of two principal types that segregate into the two regions depicted in Fig. 20: Region 1 (red colour, Tibet and the Yunnan-Guizhou plateau region) and Region 2 (blue colour, regions near the periphery of Tibet). The sedimentary basins define a third region that we do not discuss here.

Region 1: In the interior of eastern Tibet, the anisotropy of the upper crust has a steeply dipping foliation plane, which generates negative apparent radial anisotropy, and the middle-to-lower crust has a subhorizontal foliation in which the dip angle θ is often indistinguishable from zero. This results in a large positive apparent Vs radial anisotropy in the lower crust. Tibet itself has high seismicity with earthquakes occurring to a depth of about $15-20$ km within Tibet (Chu *et al.* 2009; Zhang *et al.* 2010; Sloan *et al.* 2011). Therefore, the upper crust to this depth probably undergoes brittle deformation. Steeply dipping foliation could result from fractures or faults that are subvertical or steeply dipping. In contrast, the nearly horizontal foliation plane of the middle-to-lower crust may result from the deeper crust undergoing predominantly horizontal ductile deformation in which melt-rich layers or planar mica sheets form in response to the deformation. Interestingly, this pattern of anisotropy is not unique to Tibet, but is also observed south of the Sichuan basin in the Yunnan-Guizhou Plateau.
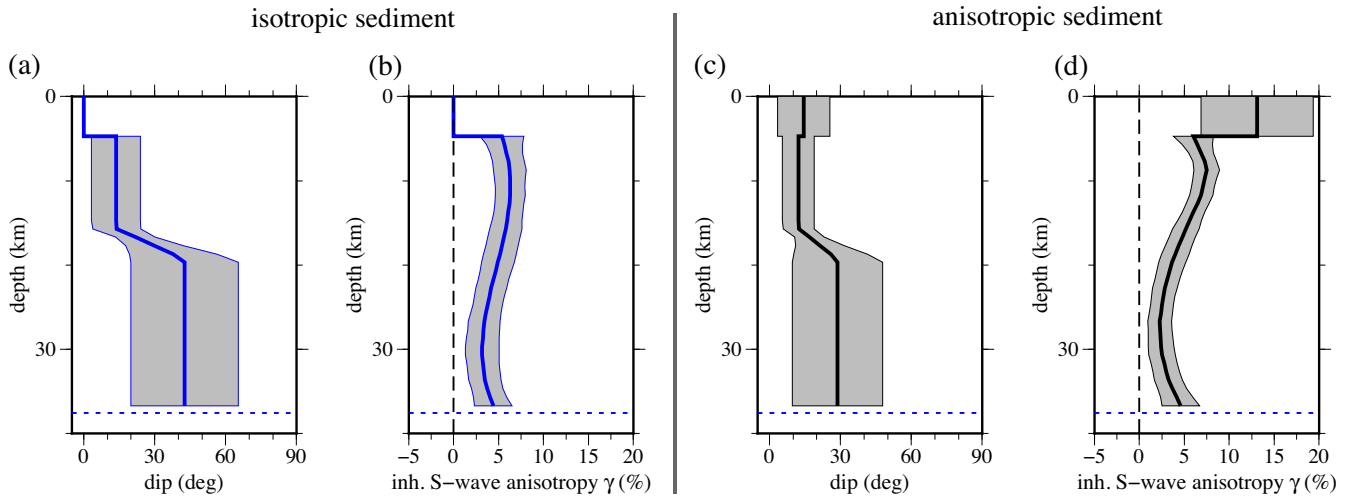
Figure 21. (a) and (b) Posterior distributions of estimated dip angle θ and inherent *S*-wave anisotropy γ for a point in the Sichuan basin (105° and 31°) presented as in Fig. 11 with no anisotropy in the sediments. (c) and (d) Posterior distributions at the same location where anisotropy and an independent dip angle is allowed in the sediments.

Region 2: Near the boundary of eastern Tibet and regions north of Tibet, such as the Qilian terrane, anisotropy has a depth constant moderate dip angle through the entire crust that results in negative to slightly positive apparent radial anisotropy throughout the crust. From Region 1 to Region 2, the orientation of the middle-to-lower crustal foliation plane rotates from horizontal to moderately or steeply dipping. This lateral change of orientation may result from resistance forces applied by the rigid and relatively undeformed Sichuan basin, Yangtze craton and Ordos block.

6.2.2 Physical significance

Our principal results are represented with a pair of variables at each location and depth from which we can compute apparent radial and azimuthal anisotropy: inherent *S*-wave anisotropy γ and dip angle θ. These variables allow us to predict the primary aspects of our observations. However, there are many constraints and assumptions underlying these results. Perhaps most significant among these is the assumption that the elastic tensor at all depths in the crust possesses hexagonal symmetry with a slow symmetry axis.

There are reasons to believe that hexagonal symmetry is a reasonable assumption for the crust. The cause of crustal anisotropy is related to shape-preferred orientation (SPO) and LPO or crystal-preferred orientation (CPO) of Earth's materials. In the crust, SPO can be caused by fluid-filled cracks and layering of materials with different compositions (e.g. Crampin 1984), and both situations can be approximated with a hexagonally symmetric medium with a slow symmetry axis. Other than SPO, another possible cause of seismic anisotropy is CPO of the crystallographic axes of elastically anisotropic minerals. Mica and amphibole are primary candidates for crustal anisotropy (Mainprice & Nicolas 1989). With increasing mica content, a deformed rock becomes anisotropic and tends to be approximately hexagonally symmetric with a slow symmetry axis (Weiss *et al.* 1999; Shao *et al.* 2016). Weiss *et al.* (1999) argue that most deep crustal rocks are quasi-hexagonal, although some studies (e.g. Tatham *et al.* 2008) conclude that the deep continental crust contains little mica, and amphibole is a more plausible explanation for deep crustal anisotropy. The presence of amphibole would reduce a rock's overall symmetry from hexagonal to a lower

symmetry such as orthorhombic (Shao *et al.* 2016). Therefore, in many cases, a hexagonally symmetric medium with a slow symmetry axis is a reasonable approximation for crustal material, and in this circumstance, the inferred dip and strike angles probably represent the orientation of the foliated anisotropic materials in the crust. But in the presence of abundant amphiboles, orthorhombic rather than hexagonal symmetry may be more appropriate. In this case, for example, it would not be clear how to interpret the estimated dip angle, which could be understood as a proxy for deviation from hexagonal symmetry.

Even when hexagonal symmetry is an appropriate assumption for the anisotropy of crustal rocks, the dip and strikes angles shown in Figs 12 and 14 represent only one of several possible orientations that are consistent with surface wave data. Xie *et al.* (2015) point out that there are two principal ambiguities in orientation that arise using surface wave data alone to estimate a depth-dependent THS model. First, there is the dip ambiguity that results from a symmetry or a pure geometrical trade-off. Surface waves are not capable of distinguishing between structures with dip angle θ and angle $180° - \theta$ (i.e. left and right dippings). As a result, surface waves cannot distinguish between a structure that dips only toward one-side from a fold that is composed of a combination of left- and right-dipping foliations. Secondly, there is the strike ambiguity. Surface waves do not distinguish between anisotropic structures that differ in strike angle by 90°. This is not a geometrical symmetry but emerges because of covariances between the elastic moduli, and is related to the so-called ellipticity of the elastic tensor, as discussed in Xie *et al.* (2015). We have eliminated this ambiguity by narrowing the range of η considered but show both strike angles in Fig. 13. The limitation we imposed on the allowed η values does not affect our principal conclusions. However, it will be important in the future to attempt to distinguish between the two strike angles by invoking other data (e.g. receiver function observations).

6.2.3 Sedimentary basins

As discussed in Section 4, we parametrized sedimentary basins as isotropic even though our data present evidence that the sediments
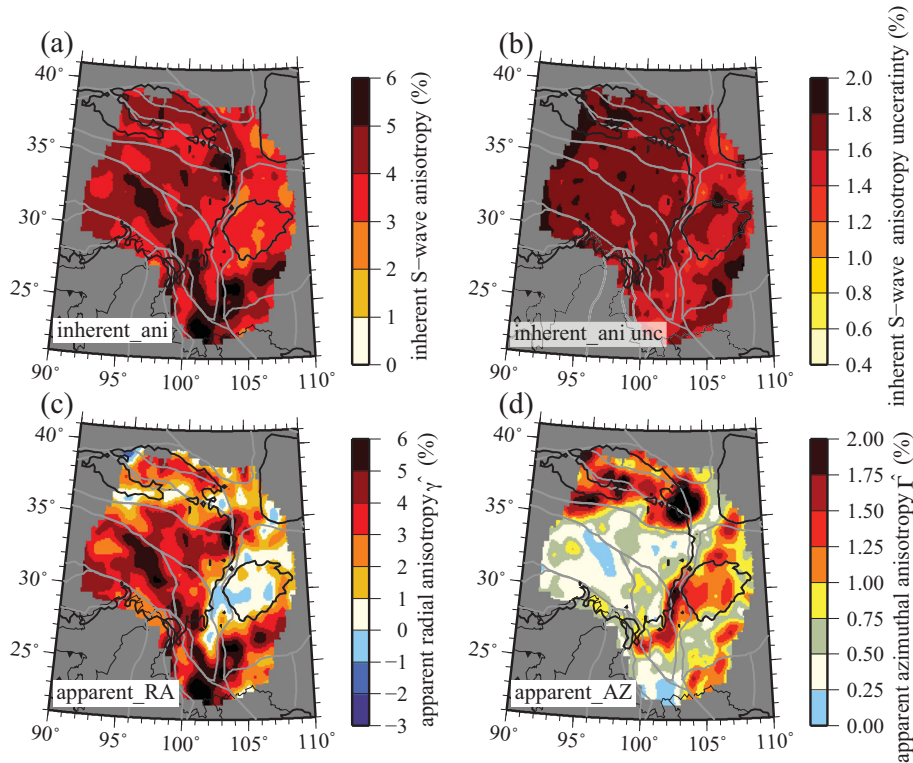
Figure 22. Aspects of inherent and apparent anisotropy estimated at a depth 5 km above the Moho: (a) inherent *S*-wave anisotropy γ, (b) standard deviation of the posterior distribution for γ, (c) apparent radial anisotropy $\hat{\gamma}$ and (d) apparent azimuthal anisotropy $\hat{\Gamma}$.

are anisotropic, as seen clearly by significant data misfit for the Sichuan and Qaidam basins in Fig. 15.

Fig. 21 presents a comparison of the results of inversion of our data at a point in the Sichuan basin (105°, 31°) with (Figs 21c and d) and without (Figs 21a and b) anisotropy in the sediments. Misfit ($S^{1/2}$, eq. 8) reduces from 3.44 to 1.40 with the introduction of anisotropy in the sediments at this point. The inherent *S*-wave anisotropy in the sediments is exceptionally strong (~13 per cent) and the dip angle is shallow. Thus, the sediments dominantly produce apparent radial anisotropy with little associated apparent azimuthal anisotropy. Including anisotropy in the sediments does not strongly change inherent *S*-wave anisotropy in the crystalline crust (Figs 21a and c) It does, however, reduce the lower crustal dip angle by about 10°. However, these changes are within the estimated uncertainties. These results are similar to what we find at other locations within the Sichuan and Qaidam basins where surface wave observations are reliable and the sediments are thicker than 2 km in the reference model.

We conclude, therefore, that the specification of isotropic sediments changes our estimates of inherent *S*-wave anisotropy and dip angle in the crystalline crust within stated uncertainties, and does not modify the primary conclusions of the study. In the future, parametrizing the sediments to include anisotropy is recommended, but in doing so it is also advisable to include other constraints on sedimentary structure such as receiver functions or Rayleigh wave *H/V* to improve the estimate of sedimentary thickness. Uncertainties in the thickness of sediments directly affect estimates of the inherent anisotropy of the sediments. For example, at the point shown in Fig. 21, our reference model (Shen *et al.* 2016) indicates a sedimentary thickness of about 4 km. If the sediments were actually thicker, then the estimate of the inherent *S*-wave anisotropy would be

smaller. Uncertainty in sedimentary thickness is one of the reasons we do not highlight structure in the basins in this paper.

6.3 Comparison with other studies

6.3.1 Vertical distribution of anisotropy in the crust

Figs 14(c) and (d) show that the strength of inherent *S*-wave anisotropy is stronger in the middle-to-lower crust than in the upper crust across most of the study region. A comparison of Figs 12(b) and (d) similarly shows this trend. To illustrate this trend, Fig. 22(a) presents inherent *S*-wave anisotropy 5 km above Moho. Inherent *S*-wave anisotropy in the deep crust is similar to the middle crust, but stronger than the shallow crust. Figs 18(a), (c), 19(a), (b) and 22(c) illustrate that the same trend holds for apparent radial anisotropy.

The nearly constant apparent radial anisotropy from middle-to-lower crust is different from the study of Xie *et al.* (2013), which concluded that apparent radial anisotropy is strongest in the middle crust. The difference between these two studies is due to two factors. (1) Love wave observations at periods below 40 s are only weakly sensitive to shear wave speeds in the lower crust of Tibet. As a consequence, inherent *S*-wave anisotropy γ is poorly determined in the lowermost crust (Fig. 8a). (2) The study of Xie *et al.* (2013) and this paper have different parametrizations and place different constraints on anisotropy in the crust. Xie *et al.* (2013) use the azimuthally invariant parts of Rayleigh and Love waves to invert for the apparent radial anisotropy $\hat{\gamma}$ without inferring the inherent properties, and $\hat{\gamma}$ is constrained to be 0 at the Moho. In contrast, this study infers the inherent properties (e.g. γ, θ, ϕ) from which apparent radial anisotropy $\hat{\gamma}$ is then derived. Here, we require

$0 \le \gamma \le 10$ per cent and the discontinuity in θ determines the resulting $\hat{\gamma}$. The result is that Xie *et al.* (2013) attempt to find a model that fits their data while minimizing lower crustal anisotropy whereas this study applies the weak anisotropy constraint across the entire crust. The differences between the results of these two studies illustrate that the strength of anisotropy below about 50 km depth cannot be determined by the data alone, but is shaped largely by constraints imposed in the inversion. Better determination of the amplitude of inherent *S*-wave anisotropy in the Tibetan lower crust will require Love wave observations at periods longer than 40 s. Such measurements will probably derive from earthquake-based observations rather than ambient noise.

6.3.2 Other aspects of the model

Many studies of Tibet might meaningfully be compared with the results we present here. We briefly discuss comparisons with three general types of studies: (1) studies that have identified differences between northern and southern Tibet, (2) studies that attempt to draw conclusions about the vertical distribution of strain near the southeast border of Tibet in the Chuandian terrane or Yunnan-Guizhou plateau and (3) receiver function studies that attempt to produce information about crustal anisotropy.

(1) Differences between northern and southern Tibet have been widely observed in other studies. Shear wave splitting studies (e.g. McNamara *et al.* 1994; Hirn *et al.* 1995; Huang *et al.* 2000) find a systematic rotation of the fast azimuth from southern to northern Tibet. Compared with southern Tibet, slower shear wave speeds (e.g. Yang *et al.* 2012) and slower *Pn* velocities (e.g. McNamara *et al.* 1997) are observed in northern Tibet. Some studies (e.g. Huang *et al.* 2000; Nábělek *et al.* 2009) suggest that 32°N marks the northern end of the subducted Indian plate. Although our study region only covers the eastern part of Tibet, we also observe differences between northern and southern Tibet on the western side of our study region. For example, compared with the southern part of our study region (Qiangtang terrane), the northern part (Songpan-Ganzi) has a steeper upper crustal dip angle (Figs 12a and 14b) and stronger middle crustal inherent anisotropy (Figs 12d and 14d).

(2) In southeastern Tibet (near the Chuandian terrane and the Yunnan-Guizhou plateau), the deformation mechanism remains under debate. Shear wave splitting studies observe a sharp transition in mantle anisotropy across about 25°N latitude. North of this boundary the fast polarization orientation is mostly north–south, which is consistent with surface strain, while in the south the fast polarization orientation changes suddenly to east–west, which deviates from the surface strain (Lev *et al.* 2006; Sol *et al.* 2007). Such deviation was used as evidence for the decoupling between the crust and mantle near the southeastern edge of Tibet because shear wave splitting is mainly caused by mantle anisotropy.

We find a similar pattern of spatial variation in Rayleigh wave fast-axis orientations in this region. For the northern part of southeastern Tibet, Rayleigh wave fast axes are nearly constant with period lying within about 20° of north–south (e.g. Fig. 5i, Point C), while south of 25°N latitude the fast azimuth is more complicated. It remains oriented north–south at short periods but changes to more nearly east–west at longer periods (e.g. Fig. 5l, Point D; Figs 3c and d). In our model, the crustal strike typically follows the Rayleigh wave fast azimuth at short periods (Figs 3c and 13a), and the mantle fast azimuth follows the Rayleigh wave fast azimuth at long periods.

We tend not to attribute the different fast-axis orientations between the crust and upper mantle to decoupling between crustal and mantle strains for several reasons. First, as pointed out by Wang *et al.* (2008) and Fouch & Rondenay (2006), anisotropy may manifest in the crust and mantle in very different ways for the same stress geometry. For example, crustal open cracks might align orthogonal to the direction of maximum extension, while in the mantle the fast direction of relatively dry olivine might align parallel to the maximum extension direction. Secondly, the possible existence of water or melt could make the interpretation more complicated (e.g. Holtzman *et al.* 2003; Kawakatsu *et al.* 2009). Moreover, as discussed in Section 6.2.2 and by Xie *et al.* (2015), the Rayleigh wave fast azimuth and strike orientations of anisotropy are ambiguously related to one another if non-ellipticity of anisotropy is allowed. Therefore, it is hazardous to draw conclusions on the coupling or decoupling of the crust and mantle deformation based on seismic anisotropy observations alone. However, Shen *et al.* (2005) argue that southeastern Tibet has a weak lower crust underlying a stronger, highly fragmented upper crust by analysing GPS data. This could provide a possible mechanism to decouple the upper crust from the upper mantle.

(3) The tilted hexagonally symmetric (THS) model that we produce is qualitatively similar to that inferred by some receiver function studies. For example, in central Tibet, Ozacar & Zandt (2004) used receiver functions to study the tilt of crustal anisotropy, and found that near-surface anisotropy has a steeply dipping fabric ($\sim$60°–80°), while mid-crustal anisotropy has a shallowly dipping fabric ($\sim$18°). This result qualitatively agrees with our findings across most of eastern Tibet. In addition, the strike angles of our THS model (and the fast directions of the short-period Rayleigh waves) are parallel to the fast-axis orientations revealed by the Moho *Ps* splitting near the eastern edge of the high plateau (e.g. Sun *et al.* 2015b; Kong *et al.* 2016). Sun *et al.* (2015b) further suggested that lower crustal flow may extrude upward into the upper crust along the steeply dipping strike faults under the Longmenshan area at the edge of the Sichuan Basin (fig. 9 in their paper), resulting in the surface uplift of the Longmenshan. Our observation of a rapid change of dip angle of the THS system from subhorizontal to subvertical beneath the same area (Fig. 12c) is consistent with this suggestion.

7 SUMMARY AND CONCLUSIONS

With ambient noise data recorded at CEArray, China Array and PASSCAL stations that are located across eastern Tibet and adjacent areas, we measure Love and Rayleigh wave isotropic phase speeds and Rayleigh wave azimuthal anisotropy. In order to explain these observations jointly, we apply a method that inverts for the properties of an anisotropic crust represented by depth-dependent THS elastic tensors. We perform the inversion with a Bayesian Monte Carlo method that produces depth-dependent marginal posterior distributions for the five inherent elastic moduli (*A*, *C*, *N*, *L* and *F* or η) as well as dip and strike angles on a 0.5° × 0.5° spatial grid. The final 3-D model is composed of the mean and standard deviation of each of these model variables.

The paper is motivated by the three questions listed in the Introduction, which are answered here. (1) Observations of apparent radial and apparent azimuthal anisotropy from surface waves can, indeed, be fit well with the oriented hexagonally symmetric elastic tensor model, analogous to the fit of similar data across the western US (Xie *et al.* 2015). The principal exception to this

finding is that to fit the data well within the Sichuan and Qaidam basins, we would have needed to introduce very strong anisotropy in the sediments (Fig. 21), which was beyond the scope of this paper. (2) In contrast to results in the western US, we find that the data across much of the study region could not be fit with a single orientation for the elastic tensor at all depths in the crust. Specifically, we find that two dip angles (one in the upper crust and the other in the middle-to-lower crust) are needed in Tibet and the Yunnan-Guizhou plateau. However, a single strike angle in the crust does suffice to allow the data to be fit across the study region. (3) The vertical distribution of anisotropy within Tibet is similar to that beneath the Yunnan-Guizhou plateau, but both regions differ from the periphery of Tibet where only a single dip angle is needed.

Our results, therefore, segregate the area of study into two regions based on crustal anisotropy, as shown in Fig. 20. Region 1 includes the interior of eastern Tibet and the Yunnan-Guizhou plateau. In this region, steeply dipping upper crustal fabric overlies shallowly dipping middle-to-lower crustal fabric and inherent *S*-wave anisotropy γ (eq. 5) is strong throughout the crust with larger amplitudes in the middle-to-lower crust. As a result, there is a vertical dichotomoy between apparent radial anisotropy $\hat{\gamma}$ (eq. 6) and apparent azimuthal anisotropy $\hat{\Gamma}$ (eq. 7). $\hat{\gamma}$ tends to be weak and negative in the upper crust and is strong and positive in the middle-to-lower crust, while $\hat{\Gamma}$ is strong mostly in the upper crust. The steep dip to the symmetry axis in the upper crust may result from fractures or faults that are subvertical or steeply dipping. In contrast, the subhorizontal or shallow dipping symmetry axes in the middle-to-lower crust may result from ductile deformation that aligns the orientation of anisotropic minerals such as mica. Region 2 covers the edge of eastern Tibet and regions north of Tibet where the foliation across entire crust has a moderate to steep dip angle and inherent *S*-wave anisotropy γ does not change strongly with depth. As a result, apparent radial anisotropy $\hat{\gamma}$ is negative to slightly positive through the entire crust, and apparent azimuthal anisotropy $\hat{\Gamma}$ is strong throughout the crust. The more steeply dipping foliation planes of anisotropy may be caused by the reorientation of anisotropic minerals as crustal flows rotate and shear near the border of Tibet, which may result from resistance forces imposed by the more rigid and relatively undeformed surroundings to Tibet.

In the future, the introduction of other data sets may improve the current model, which is based exclusively on surface waves from ambient noise. Such information may provide new insights into crustal and mantle deformation and the generation of more realistic petrologic models that agree with the elastic tensors inferred. (1) Azimuthal variations in receiver functions (e.g. Levin & Park 1997, 1998; Ozacar & Zandt 2004, 2009; Schulte-Pelkum & Mahan 2014a,b) as well as the splitting of the *P*-to-*S* converted phase (e.g. Rümpker *et al.* 2014; Sun *et al.* 2015a) can provide important point constraints on crustal anisotropy and could also help to identify depths at which crustal anisotropy changes dip angle. In some areas receiver function waveforms observe clear azimuthal variations, and these waveforms could be inverted simultaneously for the layered THS system (e.g. Ozacar & Zandt 2004; Schulte-Pelkum & Mahan 2014b) together with surface wave data. (2) Rayleigh wave *H/V* ratio provides sensitivity to the velocity structure at shallow depths (upper ∼5 km), and would help to resolve anisotropy in the sedimentary basins. (3) Shear wave splitting, both SKS and the splitting of Moho converted *P*-to-*S* phases, could be combined with surface wave data to provide additional constraints on the depth-integrated amplitude of apparent azimuthal anisotropy (e.g. Montagner *et al.* 2000; Lin *et al.* 2011). (4) In addition, longer pe-

riod surface wave measurements are needed to improve estimates of mantle anisotropy, including the type of anisotropy (e.g. hexagonal symmetry with a fast or slow symmetry axis, orthorhombic symmetry) and the orientation of the anisotropic media.

REFERENCES

Acton, C.E., Priestley, K., Gaur, V.K. & Rai, S.S., 2010. Group velocity tomography of the Indo-Eurasian collision zone, *J. geophys. Res.,* **115**(B12), B12335, doi:10.1029/2009JB007021.

Agius, M.R. & Lebedev, S., 2014. Shear-velocity structure, radial anisotropy and dynamics of the Tibetan crust, *Geophys. J. Int.,* **199**(3), 1395–1415.

Auld, B.A., 1973. *Acoustic Fields and Waves in Solids,* Wiley.

Barmin, M.P., Ritzwoller, M.H. & Levshin, A.L., 2001. A fast and reliable method for surface wave tomography, *Pure appl. Geophys.,* **158**(8), 1351–1375.

Beaumont, C., Jamieson, R.A., Nguyen, M.H. & Lee, B., 2001. Himalayan tectonics explained by extrusion of a low-viscosity crustal channel coupled to focused surface denudation, *Nature,* **414**(6865), 738–742.

Bensen, G.D., Ritzwoller, M.H., Barmin, M.P., Levshin, A.L., Lin, F., Moschetti, M.P., Shapiro, N.M. & Yang, Y., 2007. Processing seismic ambient noise data to obtain reliable broad-band surface wave dispersion measurements, *Geophys. J. Int.,* **169**(3), 1239–1260.

Bollinger, L., Henry, P. & Avouac, J., 2006. Mountain building in the Nepal Himalaya: thermal and kinematic model, *Earth planet. Sci. Lett.,* **244**(1–2), 58–71.

Brownlee, S.J., Hacker, B.R., Salisbury, M., Seward, G., Little, T.A., Baldwin, S.L. & Abers, G.A., 2011. Predicted velocity and density structure of the exhuming Papua New Guinea ultrahigh-pressure terrane, *J. geophys. Res.,* **116**(B8), B08206, doi:10.1029/2011JB008195.

Caldwell, W.B., Klemperer, S.L., Rai, S.S. & Lawrence, J.F., 2009. Partial melt in the upper-middle crust of the northwest Himalaya revealed by Rayleigh wave dispersion, *Tectonophysics,* **477**(1–2), 58–65.

Carcione, J.J.M., 2007. *Wave Fields in Real Media: Wave Propagation in Anisotropic, Anelastic, Porous and Electromagnetic Media,* Elsevier.

Chen, Y., Badal, J. & Zhang, Z., 2009. Radial anisotropy in the crust and upper mantle beneath the Qinghai-Tibet Plateau and surrounding regions, *J. Asian Earth Sci.,* **36**(4–5), 289–302.

Christensen, N.I., 1984. The magnitude, symmetry and origin of upper mantle anisotropy based on fabric analyses of ultramafic tectonites, *Geophys. J. Int.,* **76**(1), 89–111.

Chu, R., Zhu, L. & Helmberger, D.V., 2009. Determination of earthquake focal depths and source time functions in central Asia using teleseismic *P* waveforms, *Geophys. Res. Lett.,* **36,** doi:10.1029/2009GL039494.

Clark, M.K. & Royden, L.H., 2000. Topographic ooze: building the eastern margin of Tibet by lower crustal flow, *Geology,* **28**(8), 703–706.

Copley, A., Avouac, J.-P. & Wernicke, B.P., 2011. Evidence for mechanical coupling and strong Indian lower crust beneath southern Tibet, *Nature,* **472**(7341), 79–81.

Cotte, N., Pedersen, H., Campillo, M., Mars, J., Ni, J.F., Kind, R., Sandvol, E. & Zhao, W., 1999. Determination of the crustal structure in southern Tibet by dispersion and amplitude analysis of Rayleigh waves, *Geophys. J. Int.,* **138**(3), 809–819.

Crampin, S., 1984. Effective anisotropic elastic constants for wave propagation through cracked solids, *Geophys. J. Int.,* **76**(1), 135–145.

Deng, Y., Shen, W., Xu, T. & Ritzwoller, M.H., 2015. Crustal layering in northeastern Tibet: a case study based on joint inversion of receiver functions and surface wave dispersion, *Geophys. J. Int.,* **203**(1), 692–706.

Duret, F., Shapiro, N.M., Cao, Z., Levin, V., Molnar, P. & Roecker, S., 2010. Surface wave dispersion across Tibet: direct evidence for radial anisotropy in the crust, *Geophys. Res. Lett.,* **37**(16), L16306, doi:10.1029/2010GL043811.

England, P. & Molnar, P., 1997. Active deformation of Asia: from kinematics to dynamics, *Science,* **278**(5338), 647–650.

Erdman, M.E., Hacker, B.R., Zandt, G. & Seward, G., 2013. Seismic anisotropy of the crust: electron-backscatter diffraction measurements from the Basin and Range, *Geophys. J. Int.,* **195**(2), 1211–1229.

Fouch, M.J. & Rondenay, S., 2006. Seismic anisotropy beneath stable continental interiors, *Phys. Earth planet. Inter.,* **158**(2–4), 292–320.

Francheteau, J., Jaupart, C., Jie, S.X., Wen-Hua, K., De-Lu, L., Jia-Chi, B., Hung-Pin, W. & Hsia-Yeu, D., 1984. High heat flow in southern Tibet, *Nature,* **307**(5946), 32–36.

French, S.W. & Romanowicz, B.A., 2014. Whole-mantle radially anisotropic shear velocity structure from spectral-element waveform tomography, *Geophys. J. Int.,* **199**(3), 1303–1327.

Guo, Z., Gao, X., Wang, W. & Yao, Z., 2012. Upper- and mid-crustal radial anisotropy beneath the central Himalaya and southern Tibet from seismic ambient noise tomography, *Geophys. J. Int.,* **189**(2), 1169–1182.

Guo, Z., Gao, X., Yao, H., Li, J. & Wang, W., 2009. Midcrustal low-velocity layer beneath the central Himalaya and southern Tibet revealed by ambient noise array tomography, *Geochem. Geophys. Geosyst.,* **10**(5), Q05007, doi:10.1029/2009GC002458.

Hacker, B.R., Ritzwoller, M.H. & Xie, J., 2014. Partially melted, mica-bearing crust in Central Tibet, *Tectonics,* **33**(7), 1408–1424.

Hinsbergen, D.J.J., van Lippert, P.C., Dupont-Nivet, G., McQuarrie, N., Doubrovine, P.V., Spakman, W. & Torsvik, T.H., 2012. Greater India Basin hypothesis and a two-stage Cenozoic collision between India and Asia, *Proc. Natl. Acad. Sci.,* doi:10.1073/pnas.1117262109.

Hirn, A. *et al.*, 1995. Seismic anisotropy as an indicator of mantle flow beneath the Himalayas and Tibet, *Nature,* **375**(6532), 571–574.

Holtzman, B.K., Kohlstedt, D.L., Zimmerman, M.E., Heidelbach, F., Hiraga, T. & Hustoft, J., 2003. Melt segregation and strain partitioning: implications for seismic anisotropy and mantle flow, *Science,* **301**(5637), 1227–1230.

Houseman, G. & England, P., 1993. Crustal thickening versus lateral expulsion in the Indian-Asian continental collision, *J. geophys. Res.,* **98**(B7), 12 233–12 249.

Huang, H., Yao, H. & van der Hilst, R.D., 2010. Radial anisotropy in the crust of SE Tibet and SW China from ambient noise interferometry, *Geophys. Res. Lett.,* **37**, L21310, doi:10.1029/2010GL044981.

Huang, W.-C. *et al.*, 2000. Seismic polarization anisotropy beneath the central Tibetan Plateau, *J. geophys. Res.,* **105**(B12), 27 979–27 989.

Jiang, M., Zhou, S., Sandvol, E., Chen, X., Liang, X., Chen, Y.J. & Fan, W., 2011. 3-D lithospheric structure beneath southern Tibet from Rayleigh-wave tomography with a 2-D seismic array, *Geophys. J. Int.,* **185**(2), 593–608.

Jolivet, L., Davy, P. & Cobbold, P., 1990. Right-lateral shear along the Northwest Pacific Margin and the India-Eurasia Collision, *Tectonics,* **9**(6), 1409–1419.

Kang, D., Shen, W., Ning, J. & Ritzwoller, M.H., 2015. Seismic evidence for lithospheric modification associated with intracontinental volcanism in Northeastern China, *Geophys. J. Int.,* **204**(1), 215–235.

Kawakatsu, H., Kumar, P., Takei, Y., Shinohara, M., Kanazawa, T., Araki, E. & Suyehiro, K., 2009. Seismic evidence for sharp lithosphere-asthenosphere boundaries of oceanic plates, *Science,* **324**(5926), 499–502.

Kennett, B.L.N., Engdahl, E.R. & Buland, R., 1995. Constraints on seismic velocities in the Earth from traveltimes, *Geophys. J. Int.,* **122**(1), 108–124.

Kind, R. *et al.*, 1996. Evidence from earthquake data for a partially molten crustal layer in southern Tibet, *Science,* **274**(5293), 1692–1694.

Kind, R. *et al.*, 2002. Seismic images of crust and upper mantle beneath Tibet: evidence for Eurasian plate subduction, *Science,* **298**(5596), 1219–1221.

Kong, F., Wu, J., Liu, K.H. & Gao, S.S., 2016. Crustal anisotropy and ductile flow beneath the eastern Tibetan Plateau and adjacent areas, *Earth planet. Sci. Lett.,* **442,** 72–79.

Le Fort, P., 1975. Himalayas, the collided range: present Knowledge of the continental arc, *Am. J. Sci.,* **275A,** 1–44.

Lev, E., Long, M.D. & van der Hilst, R.D., 2006. Seismic anisotropy in Eastern Tibet from shear wave splitting reveals changes in lithospheric deformation, *Earth planet. Sci. Lett.,* **251**(3–4), 293–304.

Levin, V. & Park, J., 1997. P-SH conversions in a flat-layered medium with anisotropy of arbitrary orientation, *Geophys. J. Int.,* **131,** 53–266.

Levin, V. & Park, J., 1998. P-SH conversions in layered media with hexagonally symmetric anisotropy: a cookbook, *Pure appl. Geophys.,* **151,** 669–697.

Levshin, A.L. & Ritzwoller, M.H., 2001. Automated detection, extraction, and measurement of regional surface waves, *Pure appl. Geophys.,* **158**(8), 1531–1545.

Li, H., Su, W., Wang, C.-Y. & Huang, Z., 2009. Ambient noise Rayleigh wave tomography in western Sichuan and eastern Tibet, *Earth planet. Sci. Lett.,* **282**(1–4), 201–211.

Li, X., Wei, D., Yuan, X., Kind, R., Kumar, P. & Zhou, H., 2011. Details of the doublet Moho structure beneath Lhasa, Tibet, obtained by comparison of P and S receiver functions, *Bull. seism. Soc. Am.,* **101**(3), 1259–1269.

Lin, F.-C. & Ritzwoller, M.H., 2011. Helmholtz surface wave tomography for isotropic and azimuthally anisotropic structure, *Geophys. J. Int.,* **186**(3), 1104–1120.

Lin, F.-C., Ritzwoller, M.H. & Snieder, R., 2009. Eikonal tomography: surface wave tomography by phase front tracking across a regional broadband seismic array, *Geophys. J. Int.,* **177**(3), 1091–1110.

Lin, F.-C., Ritzwoller, M.H., Yang, Y., Moschetti, M.P. & Fouch, M.J., 2011. Complex and variable crustal and uppermost mantle seismic anisotropy in the western United States, *Nat. Geosci.,* **4**(1), 55–61.

Mainprice, D. & Nicolas, A., 1989. Development of shape and lattice preferred orientations: application to the seismic anisotropy of the lower crust, *J. Struct. Geol.,* **11**(1–2), 175–189.

Marone, F. & Romanowicz, B., 2007. The depth distribution of azimuthal anisotropy in the continental upper mantle, *Nature,* **447**(7141), 198–201.

Marone, F., Gung, Y. & Romanowicz, B., 2007. Three-dimensional radial anisotropic structure of the North American upper mantle from inversion of surface waveform data, *Geophys. J. Int.,* **171**(1), 206–222.

McNamara, D., Owens, T., Silver, P. & Wu, F., 1994. Shear-wave anisotropy beneath the Tibetan plateau, *J. geophys. Res.,* **99**(B7), 13 655–13 665.

McNamara, D.E., Walter, W.R., Owens, T.J. & Ammon, C.J., 1997. Upper mantle velocity structure beneath the Tibetan Plateau from Pn travel time tomography, *J. geophys. Res.,* **102**(B1), 493–505.

Molnar, P. & Tapponnier, P., 1975. Cenozoic tectonics of Asia: effects of a continental collision, *Science,* **189**(4201), 419–426.

Montagner, J.-P. & Jobert, N., 1988. Vectorial tomography—II. Application to the Indian Ocean, *Geophys. J. Int.,* **94**(2), 309–344.

Montagner, J.-P. & Nataf, H.-C., 1986. A simple method for inverting the azimuthal anisotropy of surface waves, *J. geophys. Res.,* **91**(B1), 511–520.

Montagner, J.-P. & Nataf, H.-C., 1988. Vectorial tomography—I. Theory, *Geophys. J. Int.,* **94**(2), 295–307.

Montagner, J.-P., Griot-Pommera, D.-A. & Lavé, J., 2000. How to relate body wave and surface wave anisotropy?, *J. geophys. Res.,* **105**(B8), 19 015–19 027.

Moschetti, M.P., Ritzwoller, M.H., Lin, F. & Yang, Y., 2010. Seismic evidence for widespread western-US deep-crustal deformation caused by extension, *Nature,* **464**(7290), 885–889.

Nábĕlek, J. *et al.*, 2009. Underplating in the Himalaya-Tibet collision zone revealed by the Hi-CLIMB experiment, *Science,* **325**(5946), 1371–1374.

Nelson, K.D. *et al.*, 1996. Partially molten middle crust beneath southern Tibet: synthesis of project INDEPTH results, *Science,* **274**(5293), 1684–1688.

Nettles, M. & Dziewoński, A.M., 2008. Radially anisotropic shear velocity structure of the upper mantle globally and beneath North America, *J. geophys. Res.,* **113**, B02303, doi:10.1029/2006JB004819.

Okaya, D.A. & Christensen, N.I., 2002. Anisotropic effects of non-axial seismic wave propagation in foliated crustal rocks, *Geophys. Res. Lett.,* **29**(11), 2–1–2–4.

Ozacar, A.A. & Zandt, G., 2004. Crustal seismic anisotropy in central Tibet: implications for deformational style and flow in the crust, *Geophys. Res. Lett.,* **31**(23), L23601, doi:10.1029/2004GL021096.

Ozacar, A.A. & Zandt, G., 2009. Crustal structure and seismic anisotropy near the San Andreas Fault at Parkfield, California, *Geophys. J. Int.,* **178,** 1098–1104.

Pandey, S., Yuan, X., Debayle, E., Tilmann, F., Priestley, K. & Li, X., 2015. Depth-variant azimuthal anisotropy in Tibet revealed by surface wave tomography, *Geophys. Res. Lett.,* **42**(11), 2015GL063921, doi:10.1002/2015GL063921.

Panning, M. & Romanowicz, B., 2006. A three-dimensional radially anisotropic model of shear velocity in the whole mantle, *Geophys. J. Int.,* **167**(1), 361–379.

Rapine, R., Tilmann, F., West, M., Ni, J. & Rodgers, A., 2003. Crustal structure of northern and southern Tibet from surface wave dispersion analysis, *J. geophys. Res.,* **108**(B2), 2120, doi:10.1029/2001JB000445.

Royden, L.H., Burchfiel, B.C., King, R.W., Wang, E., Chen, Z., Shen, F. & Liu, Y., 1997. Surface deformation and lower crustal flow in Eastern Tibet, *Science,* **276**(5313), 788–790.

Rümpker, G., Kaviani, A. & Latifi, K., 2014. Ps-splitting analysis for multilayered anisotropic media by azimuthal stacking and layer stripping, *Geophys. J. Int.,* **199**(1), 146–163.

Schulte-Pelkum, V. & Mahan, K., 2014a. Imaging faults and shear zones with receiver functions, *Pure appl. Geophys.,* **171**, 2967–2991.

Schulte-Pelkum, V. & Mahan, K.H., 2014b. A method for mapping crustal deformation and anisotropy with receiver functions and first results from USArray, *Earth planet. Sci. Lett.,* **402**, 221–233.

Shao, T., Ji, S., Oya, S., Michibayashi, K. & Wang, Q., 2016. Mica-dominated seismic properties of mid-crust beneath west Yunnan (China) and geodynamic implications, *Tectonophysics,* **677**, 324–338.

Shapiro, N.M. & Ritzwoller, M.H., 2002. Monte-Carlo inversion for a global shear-velocity model of the crust and upper mantle, *Geophys. J. Int.,* **151**(1), 88–105.

Shapiro, N.M., Ritzwoller, M.H., Molnar, P. & Levin, V., 2004. Thinning and flow of Tibetan crust constrained by seismic anisotropy, *Science,* **305**(5681), 233–236.

Shen, W. & Ritzwoller, M.H., 2016. Crustal and uppermost mantle structure beneath the United States, *J. geophys. Res.,* 2016JB012887, doi:10.1002/2016JB012887.

Shen, W. *et al.*, 2016. A seismic reference model for the crust and uppermost mantle beneath China from surface wave dispersion, *Geophys. J. Int.,* **206**(2), 954–979.

Shen, W., Ritzwoller, M.H. & Schulte-Pelkum, V., 2013a. A 3-D model of the crust and uppermost mantle beneath the Central and Western US by joint inversion of receiver functions and surface wave dispersion, *J. geophys. Res.,* **118**(1), 262–276.

Shen, W., Ritzwoller, M.H. & Schulte-Pelkum, V., 2013b. Crustal and uppermost mantle structure in the central U.S. encompassing the Midcontinent Rift, *J. geophys. Res.,* **118**(8), 4325–4344.

Shen, W., Ritzwoller, M.H., Schulte-Pelkum, V. & Lin, F.-C., 2013c. Joint inversion of surface wave dispersion and receiver functions: a Bayesian Monte-Carlo approach, *Geophys. J. Int.,* **192**(2), 807–836.

Simons, F.J., Van Der Hilst, R.D., Montagner, J.-P. & Zielhuis, A., 2002. Multimode Rayleigh wave inversion for heterogeneity and azimuthal anisotropy of the Australian upper mantle, *Geophys. J. Int.,* **151**(3), 738–754.

Sloan, R.A., Jackson, J.A., McKenzie, D. & Priestley, K., 2011. Earthquake depth distributions in central Asia, and their relations with lithosphere thickness, shortening and extension, *Geophys. J. Int.,* **185**(1), 1–29.

Smith, M.L. & Dahlen, F.A., 1973. The azimuthal dependence of Love and Rayleigh wave propagation in a slightly anisotropic medium, *J. geophys. Res.,* **78**(17), 3321–3333.

Sol, S. *et al.*, 2007. Geodynamics of the southeastern Tibetan Plateau from seismic anisotropy and geodesy, *Geology,* **35**(6), 563–566.

Su, W., Wang, C. & Huang, Z., 2008. Azimuthal anisotropy of Rayleigh waves beneath the Tibetan Plateau and adjacent areas, *Sci. China Ser. Earth Sci.,* **51**(12), 1717–1725.

Sun, Y., Liu, J., Zhou, K., Chen, B. & Guo, R., 2015a. Crustal structure and deformation under the Longmenshan and its surroundings revealed by receiver function data, *Phys. Earth planet. Inter.,* **244**, 11–22.

Sun, X. *et al.*, 2015b. Crustal structure beneath SE Tibet from joint analysis of receiver functions and Rayleigh wave dispersion, *Geophys. Res. Lett.,* **41,** 1479–1484.

Tan, J., Li, H., Li, X., Zhou, M., Ouyang, L., Sun, S. & Zheng, D., 2015. Radial anisotropy in the crust beneath the northeastern Tibetan Plateau from ambient noise tomography, *J. Earth Sci.,* **26**(6), 864–871.

Tapponnier, P., Zhiqin, X., Roger, F., Meyer, B., Arnaud, N., Wittlinger, G. & Jingsui, Y., 2001. Oblique stepwise rise and growth of the Tibet plateau, *Science,* **294**(5547), 1671–1677.

Tatham, D.J., Lloyd, G.E., Butler, R.W.H. & Casey, M., 2008. Amphibole and lower crustal seismic properties, *Earth planet. Sci. Lett.,* **267**(1–2), 118–128.

Thomsen, L. & Anderson, D.L., 2015. Weak elastic anisotropy in global seismology, in *Geological Society of America Special Papers,* Vol. 514, pp. 39–50, Geological Society of America.

Tian, Y., Shen, W. & Ritzwoller, M.H., 2013. Crustal and uppermost mantle shear velocity structure adjacent to the Juan de Fuca Ridge from ambient seismic noise, *Geochem. Geophys. Geosyst.,* **14**(8), 3221–3233.

Wang, C.-Y., Flesch, L.M., Silver, P.G., Chang, L.-J. & Chan, W.W., 2008. Evidence for mechanically coupled lithosphere in central Asia and resulting implications, *Geology,* **36**(5), 363–366.

Weiss, T., Siegesmund, S., Rabbel, W., Bohlen, T. & Pohl, M., 1999. Seismic velocities and anisotropy of the lower continental crust: a review, *Pure appl. Geophys.,* **156**(1–2), 97–122.

Xie, J., Ritzwoller, M.H., Brownlee, S.J. & Hacker, B.R., 2015. Inferring the oriented elastic tensor from surface wave observations: preliminary application across the western United States, *Geophys. J. Int.,* **201**(2), 996–1021.

Xie, J., Ritzwoller, M.H., Shen, W., Yang, Y., Zheng, Y. & Zhou, L., 2013. Crustal radial anisotropy across Eastern Tibet and the Western Yangtze Craton, *J. geophys. Res.,* **118**(8), 4226–4252.

Xu, L., Rondenay, S. & van der Hilst, R.D., 2007. Structure of the crust beneath the southeastern Tibetan Plateau from teleseismic receiver functions, *Phys. Earth planet. Inter.,* **165**(3–4), 176–193.

Yang, Y., Ritzwoller, M.H., Zheng, Y., Shen, W., Levshin, A.L. & Xie, Z., 2012. A synoptic view of the distribution and connectivity of the

mid-crustal low velocity zone beneath Tibet, *J. geophys. Res.,* **117,** B04303, doi:10.1029/2011JB008810.

Yao, H., Beghein, C. & van der Hilst, R.D., 2008. Surface-wave array tomography in SE Tibet from ambient seismic noise and two-station analysis—II. Crustal and upper-mantle structure, *Geophys. J. Int.,* **173,** 205–219.

Yao, H., van der Hilst, R.D. & Montagner, J.-P., 2010. Heterogeneity and anisotropy of the lithosphere of SE Tibet from surface wave array tomography, *J. geophys. Res.,* **115**(B12), B12307, doi:10.1029/2009JB007142.

Yuan, H., Romanowicz, B., Fischer, K.M. & Abt, D., 2011. 3-D shear wave radially and azimuthally anisotropic velocity model of the North American upper mantle, *Geophys. J. Int.,* **184**(3), 1237–1260.

Zhang, P.-Z., Wen, X., Shen, Z.-K. & Chen, J., 2010. Oblique, high-angle, listric-reverse faulting and associated development of strain: the Wenchuan earthquake of May 12, 2008, Sichuan, China, *Annu. Rev. Earth Planet. Sci.,* **38**(1), 353–382.

Zheng, Y., Shen, W., Zhou, L., Yang, Y., Xie, Z. & Ritzwoller, M.H., 2011. Crust and uppermost mantle beneath the North China Craton, northeastern China, and the Sea of Japan from ambient noise tomography, *J. geophys. Res.,* **116**(B12), B12312, doi:10.1029/2011JB008637.

Zhou, L., Xie, J., Shen, W., Zheng, Y., Yang, Y., Shi, H. & Ritzwoller, M.H., 2012. The structure of the crust and uppermost mantle beneath South China from ambient noise and earthquake tomography, *Geophys. J. Int.,* **189**(3), 1565–1583.